The Astrophysical Journal, 888:100 (18pp), 2020 January 10 https://doi.org/10.3847/1538-4357/ab5e34

CME-induced Thermodynamic Changes in the Corona as Inferred from Fe XI and Fe XIV Emission Observations during the 2017 August 21 Total Solar Eclipse

Benjamin Boe[1], Shadia Habbal[1], Miloslav Druckmüller[2], Adalbert Ding[3,4], Jana Hodérova[2], and Pavel Štarha[2]
[1] Institute for Astronomy, University of Hawaii, Honolulu, HI 96822, USA; bboe@hawaii.edu
[2] Faculty of Mechanical Engineering, Brno University of Technology, Technicka 2, 616 69 Brno, Czech Republic
[3] Institute of Optics and Atomic Physics, Technische Universitaet Berlin, Germany
[4] Institut für Technische Physik, Berlin, Germany
Received 2019 April 15; revised 2019 November 20; accepted 2019 November 22; published 2020 January 14

Abstract

We present the first remote sensing observations of the impact from a Coronal Mass Ejection (CME) on the thermodynamic properties of the solar corona between 1 and 3 $R_\odot$. Measurements of the Fe XI (789.2 nm) and Fe XIV (530.3 nm) emission were acquired with identical narrow-bandpass imagers at three observing sites during the 2017 August 21 Total Solar Eclipse (TSE). Additional continuum imagers were used to observe K+F corona scattering, which is critical for the diagnostics presented here. The total distance between sites along the path of totality was 1400 km, corresponding to a difference of 28 minutes between the times of totality at the first and last site. These observations were used to measure the Fe XI and Fe XIV emission relative to continuum scattering, as well as the relative abundance of Fe^{10+} and Fe^{13+} from the line ratio. The electron temperature (T_e) was then computed via theoretical ionization abundance values. We find that the range of T_e is (1.1–1.2) $\times$ 10^6 K in coronal holes and (1.2–1.4) $\times$ 10^6 K in streamers. Statistically significant changes of T_e occurred throughout much of the corona between the sites as a result of serendipitous CME activity prior to the eclipse. These results underscore the unique advantage of multi-site and multi-wavelength TSE observations for probing the dynamic and thermodynamic properties of the corona over an uninterrupted distance range from 1 to 3 $R_\odot$.

Unified Astronomy Thesaurus concepts: Total eclipses (1704); Solar eclipses (1489); Solar particle emission (1517); Solar E coronal region (1990); Solar K coronal region (2042); Solar F coronal region (1991); Solar abundances (1474); Solar coronal mass ejections (310); Solar coronal mass ejection shocks (1997); Solar coronal transients (312); Solar coronal streamers (1486); Solar coronal holes (1484)

Supporting material: animation

1. Introduction

The first indications of the high electron temperature, T_e, of the solar corona came from a previously unknown emission line that was observed during the 1869 Total Solar Eclipse (TSE) by Young (1870, 1871, 1872). This emission line was subsequently identified as Fe XIV (530.3 nm) by Grotrian (1934, 1939) and Edlén (1943). It took over six decades to recognize that the Fe XIV spectral line came from a ground state magnetic dipole transition of Fe^{13+}, whose presence implied that the coronal plasma has a $T_e > 10^6$ K. Shortly thereafter, theories emerged to explain the cause of the high T_e (e.g., magnetic wave heating; Alfvén 1947), and to predict the existence of the solar wind as a consequence of the corona's high temperature (Parker 1958). Theoretical analyses have advanced a great deal since these early models, yet they are still largely unconstrained by observational data in the corona between 1 and 3 $R_\odot$. Since T_e is one of the main parameters that coronal heating and solar wind models must attempt to reproduce, it is important to have a complete understanding of its distribution in the corona.

With the advent of space-based observations, inferences of the coronal T_e have vastly expanded via remote sensing at wavelengths that were previously inaccessible from the ground, and by in situ particle detector measurements of the solar wind. Ultraviolet and Extreme Ultraviolet (EUV) spectroscopy can be used to infer T_e in the chromosphere and low corona (<1.5 $R_\odot$) from remote sensing observations of ionic emission lines (e.g., Habbal et al. 1993; Raymond et al. 1997; Morgan & Taroyan 2017). The coronal T_e's that have been inferred from these studies typically range from 1 to 4 $\times$ 10^6 K. Particle detectors in situ, such as SWICS on *Ulysses* and *ACE*, have inferred coronal T_e via measurements of charge to mass ratios of solar wind plasma (Gloeckler et al. 1992, 1998). Ion abundance ratios are determined from charge to mass ratios, which are then modeled to infer to T_e in the corona at the freeze-in distance (e.g., Hundhausen et al. 1968; Owocki et al. 1983; Ko et al. 1997; Zurbuchen et al. 2002). The in situ measurements typically yield values between 1 and 3 $\times$ 10^6 K (Habbal et al. 2010b), which vary spatially between structures such as coronal holes and streamers, as well as with transient events such as the passage of Coronal Mass Ejections (CMEs) (Smith et al. 2003).

While they are highly valuable, inferences of T_e based on in situ and EUV measurements have some key limitations. In situ analyses face difficulties in robustly tracing the origin of the ions back to the corona (e.g., Galvin 1997), and EUV intensity drops very quickly with distance in the corona due to its dependence on the density squared (i.e., n_e^2; from collisional excitation, see Section 4.2). Furthermore, EUV imaging observations, such as those provided by *SDO*/AIA, have to contend with line crowding in the filter bandpasses, causing a highly complex temperature response function (e.g., O'Dwyer et al. 2010; Boerner et al. 2012). An iterative method is often used to settle on a best fit temperature, although this technique can produce different results with the same data depending on the exact iteration method used (Dudok de Wit et al. 2013). This technique also assumes a state of ionization equilibrium in the corona, which is not necessarily valid beyond $\approx$ 1.2 $R_\odot$, as demonstrated by Landi et al. (2012) through modeling and by

Table 1
Observing Locations and Corresponding Eclipse Parameters

Observing Site	Mitchell, OR	Mackay, ID	Alliance, NE
Latitude	N 44° 31′ 32.″34	N 44° 3′ 12.″59	N 42° 5′ 24.″30
Longitude	W 119° 54′ 27.″54	W 109° 36′ 39.″67	W 103° 0′ 29.″98
Elevation (m)	1100	1946	1300
Solar Altitude (deg)	42.5–42.8	47.6–47.9	56.5–56.8
C2 Time (UT)	17:21:11.7	17:29:53.0	17:48:57.5
C3 Time (UT)	17:23:14.1	17:32:08.0	17:51:28
Duration (minutes)	2.04	2.25	2.51

Boe et al. (2018) from inferences of Fe^{10+} (Fe XI, 789.2 nm) and Fe^{13+} (Fe XIV, 530.3 nm) freeze-in distances, which can be as low as 1.2 $R_\odot$ in coronal holes.

In this work, we use imaging observations of Fe XI and Fe XIV emission taken from three sites during the 2017 August 21 TSE, as described in Section 2. The data spanned almost 30 minutes of totality, which enabled the inference of the spatial distribution and temporal variation of the Fe XI and Fe XIV line to continuum intensity ratios (see Section 3.1), as well as the ionic density ratio and T_e in the corona using the technique described in Section 3.2. Spatial differences between coronal holes and streamers are presented in Section 4.1. An analysis of the temporal variability of coronal thermodynamical properties between observing sites and a discussion on the effect that a CME had on these observations are given in Section 4.2. Concluding remarks are given in Section 5.

2. Data

2.1. Eclipse Observations

The imaging data of the solar corona used here were acquired during the 2017 August 21 TSE at three separate sites spread over 1400 km along the path of totality in the United States. Mitchell, Oregon, was the first site to experience totality, followed by Mackay, Idaho, and finally Alliance, Nebraska, which viewed totality approximately half an hour after Mitchell. All three sites had cloudless skies and good seeing throughout totality. Details of the observing locations and eclipse conditions for each site can be found in Table 1.

Each observing site was equipped with a suite of narrowband imaging telescopes to observe optical line and continuum emission in the corona. All imagers had a 70 mm diameter aperture, a 300 mm focal length achromat lens and a 0.5 nm Fabry–Pérot bandpass filter manufactured by Andover corporation. The emission lines of Fe^{10+} (Fe XI, 789.2 nm) and Fe^{13+} (Fe XIV, 530.3 nm) were observed using filtered imaging systems centered on the wavelength of line emission, which we will refer to as "on-band" hereafter. Additional continuum, or "off-band," imagers were used to measure the continuum emission at a nearby wavelength to the line emission for both Fe XI and Fe XIV (see Section 2.2). Throughout the rest of this article we will refer to the Roman numeral version (i.e., Fe XI) when discussing the observed line emission and the ionic version (i.e., Fe^{10+}) when referring to the ions themselves.

While coronal emission lines provide the best metric for inferring T_e in the corona (see Section 3.2), the most dominant form of coronal emission at visible wavelengths is actually continuum radiation from Thompson scattering of solar photons by electrons, known as the K corona, combined with Mie scattering by dust particles, called the F corona or inner zodiacal light (van de Hulst 1950). The off-band images can be treated as a measurement of the K+F corona at a well-defined wavelength, while the on-band images capture the exact same K+F corona, albeit with the addition of forbidden ion emission lines (or E corona). These continuum observations are essential for measuring and differentiating between K+F scattering and spectral line emission (see Section 3.1). Indeed, a single imaging observation at visible or infrared wavelengths is incapable of differentiating line emission from continuum radiation. Such an observation will not provide any physically meaningful information about the corona, other than morphological structure, unless the continuum emission is also observed and subtracted.

An example of data collected from Mitchell, OR, is shown in Figure 1, including a broadband white light image that records the finely detailed structures in the corona (Figure 1(A)). Figures 1(B) and (C) show the off-band subtracted Fe XI and Fe XIV emission (see Section 2.2), followed by two composite images. The data presented in this figure were processed using the Adaptive Circular High-pass Filter (ACHF) method to enhance structural features in the corona, and therefore they are not representative of the absolute coronal brightness. The ACHF method, which was introduced by Druckmüller et al. (2006), has been used previously to process white light eclipse images (e.g., Habbal et al. 2010b, 2014; Alzate et al. 2017; Boe et al. 2018). Note that the white light image (i.e., Figure 1(A)) is not used in our analysis except to provide context for the Fe XI and Fe XIV photometric observations.

The 0.5 nm Fabry–Pérot bandpass filters were mounted at the front of each telescope's objective lens to avoid angle dependent changes to the wavelength transmission. Our total field of view is within 1° of Sun center, which corresponds to a change in wavelength transmission of about 0.1 nm based on the equation provided by the manufacturer:

$$\lambda = \lambda_0 \left(1 - \left(\frac{n_m}{n_f} \right)^2 \sin^2 \theta \right)^{0.5}, \quad (1)$$

where n_m is the refractive index of the external medium (air) and n_f is the refractive index of the filter. The wavelength shift induced by the filter with angular distance in the data is thus substantially smaller than the size of the transmission width and will not have an impact on our final results. There will also be a shift in wavelength due to the temperature of the filter. Consequently, each filter was equipped with an electric heater that maintains the temperature at a precision of 0.1 K to ensure the correct observational wavelength.

All of the Fabry–Pérot filters were designed with full width at half maximum values of 0.5 nm, but there was some small variation between the filters. We performed a theoretical test on the filter profiles by modeling the line and continuum intensity that would be measured by the exact filter profiles compared to each other, after a solar disk calibration (see Section 2.2). We find that all of the filters can recover the same on- and off-band intensity to $<1\%$ for a synthetic solar continuum combined with a 0.2 nm Gaussian line emission profile.

The Fe XIV systems had Atik 314L cameras, while Atik 414EX cameras were used with the Fe XI systems due to their higher quantum efficiency in the near-infrared. Both camera models have an array of 1400 × 1024 pixels that are each

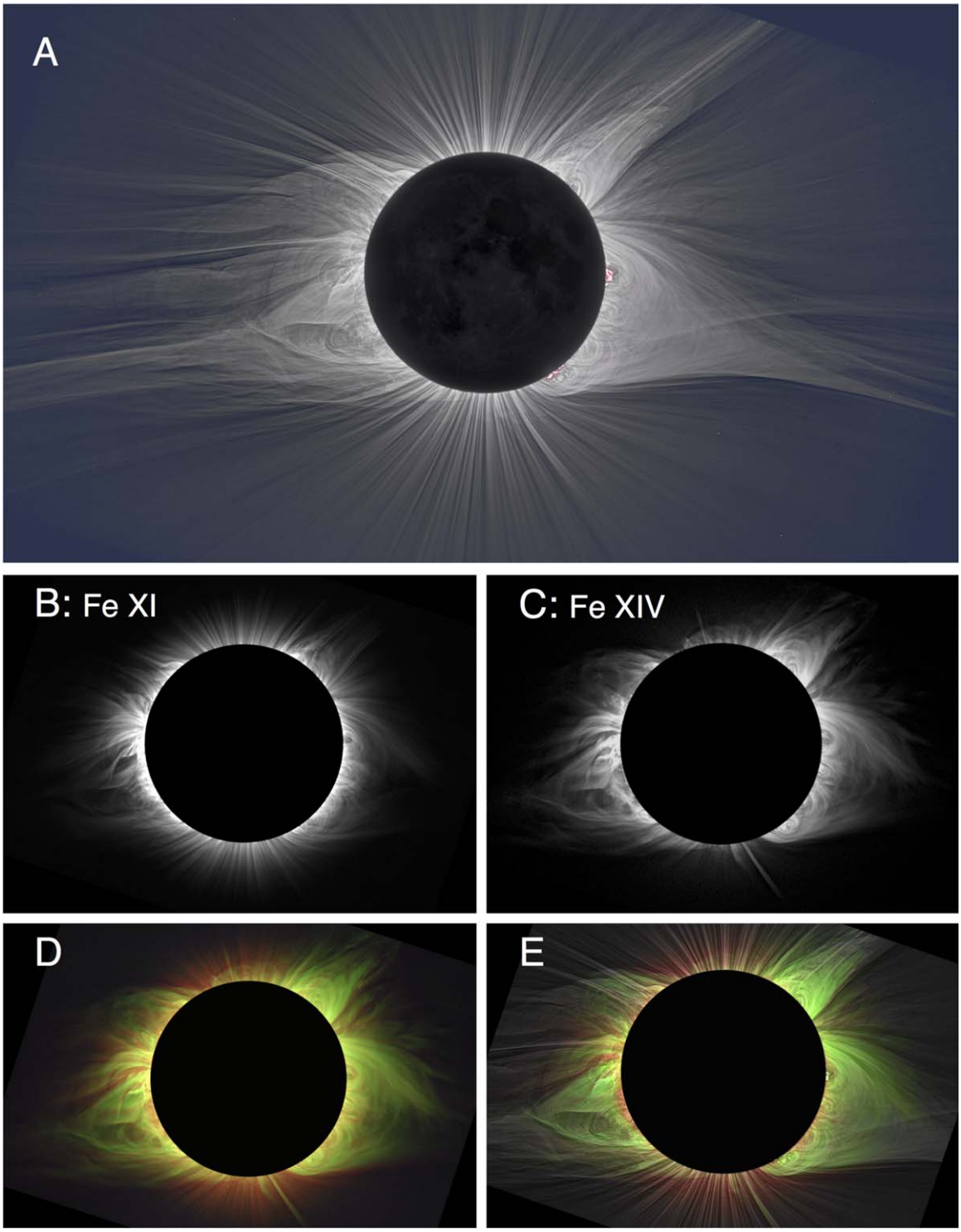

Figure 1. Total solar eclipse observations from Mitchell, OR, on 2017 August 21. Solar north is vertically up in all images. A: Processed white light image of the solar corona. B: Processed image of the Fe XI 789.2 nm emission at $\approx 1.1 \times 10^6$ K. C: Processed image of the Fe XIV 530.3 nm emission at $\approx 1.8 \times 10^6$ K. D: Composite of B (red) and C (green). E: Same as D overlaid on the white light image (note that the corresponding continuum has been subtracted from the on band Fe XI and Fe XIV images prior to processing to produce the images shown here).

6.5 μm in size, resulting in an angular resolution of about 4″ per pixel. For this work, we rebinned the original data in 2×2 pixel squares, hence increasing the signal to noise ratio at the cost of reducing spatial resolution to $\approx 8''$. Photometric uncertainties were computed using $\sigma = \sqrt{N}$, where N is the number of counts in the raw data for a given pixel. The uncertainty of any pixel intensity ratio presented in this work (e.g., Sections 3.1 and 3.2.3), was determined by propagating the individual photometric uncertainties using standard error propagation equations (e.g., for subtracted line emission, the uncertainty is the propagation of error from both the on band and continuum intensity measurements).

During totality, the cameras cycled through a sequence of seven different exposure times from 0.1 to 6.4 s, spaced by factors of two in time. A range of exposure times is required to measure the >3 orders of magnitude change of the coronal intensity between a heliocentric distance of 1 and 3 $R_\odot$. Each exposure was individually reduced using traditional dark subtraction and flat-fielding techniques. The sequence of observations were then aligned and stacked separately for each telescope system using the phase correlation method that was described in Druckmüller (2009). The sky brightness in each dataset was measured as the average surface brightness below 0.05 $R_\odot$ (in front of the Moon) and was subtracted from the data.

2.2. Data Calibration

Relative calibrations between the telescope systems at each site were made using observations of the full solar disk after the partial phases of the eclipse had ended (after C4), through an additional Neutral Density (ND) filter mounted on the telescope aperture (to reduce the intensity of the solar disk). All of the ND filters that we used were designed to attenuate the intensity to 1.5×10^{-5} of the incident intensity in the vicinity of the observed wavelength, where the same filter was used for each on- and off-band pair at given site. The entire intensity of the disk was integrated in the images (with the same reduction process used for the eclipse data) and was then used to scale the photometric response of the on- and off-band instrument pairs at each site. The size of the solar disk in the image is around 5×10^5 pixels, with each pixel having an intensity $>10^3$ counts, leading to a precise relative photometric calibration. The solar disk calibration enables a measurement of the line to continuum intensity ratio for Fe XI and Fe XIV at each site (see Section 3.1).

At Mitchell, Oregon, the continuum imagers had a central filter wavelength shifted by approximately 3 nm toward the blue relative to the emission line observations. These separations represent a Doppler velocity shift of 1200 and 1640 km s^{-1} for Fe XI and Fe XIV respectively, which is significantly higher than the speeds expected in the corona or solar wind (e.g., Smith et al. 2003; Habbal et al. 2010b). Consequently, it can be safely assumed that these continuum observations are not contaminated by Doppler shifted line emission. However, at Mackay and Alliance the filters were shifted by only 0.94 and 1.4 nm for Fe XI and Fe XIV, which correspond to a Doppler velocity of 530 km s^{-1} for both ions. It is possible for coronal and solar wind plasma to be moving at this velocity (especially in the fast solar wind where Fe^{10+} is very abundant), so Doppler shifted contamination is possible. In fact, we see strong evidence of Doppler shifted emission, especially in the Fe XI continuum data (see Appendix A).

Fortunately, at the Alliance site there was an additional continuum imager meant for the Ar X (553.3 nm) emission line. The Ar X line intensity was too faint for us to use in this work, but the Ar X continuum observation at 552.3 nm is only separated by 22 nm (>12,000 km s^{-1}) from the Fe XIV line and so is usable as a replacement for the original Fe XIV continuum observation. The 552.3 nm continuum observation also had solar disk calibration observations made with the same ND filter as used for the Fe XIV calibration, so we used the nominal procedure to calibrate this substitute data. No additional continuum data was available at the Mackay site, so we used the unaltered Fe XIV continuum data. Based on the Doppler emission seen in the Alliance Fe XIV continuum data (after having the Ar X continuum subtracted, see Appendix A), there is an average of about 5.7% Doppler contamination, with a maximum of about 12%. To account for this possible Doppler bias, we introduced an additional 5.7% uncertainty to the error analysis of the Mackay data. For both Mackay and Alliance, the solar disk calibrations are still valid for producing a pristine line to continuum ratio metric for Fe XIV (see Section 3.1).

The Fe XI data at Mackay and Alliance are more complicated to calibrate given the Doppler shifted contamination. Unlike the relatively small impact of Doppler shifted Fe XIV, the Fe XI continuum data at Mackay and Alliance show a strong contribution from Doppler shifted emission. Based on this contamination, we were forced to model the Fe XI continuum data for Mackay and Alliance using the Fe XIV and Ar X continuum data, respectively. An additional complication for creating a realistic Fe XI continuum is possible reddening effects from the F corona. The K corona will have a neutral color because Thompson scattering has no wavelength dependence whatsoever, whereas the F corona can be reddened at visible wavelengths due to dust diffraction scattering (van de Hulst 1947). The K corona is the strongest component of the continuum below at least 1.3 $R_\odot$ everywhere in the corona throughout the solar cycle (e.g., Koutchmy & Lamy 1985; Kimura & Mann 1998 and references therein), and so the continuum in the corona will *not* be substantially impacted by F corona reddening at 1.1 $R_\odot$ (Roeser & Staude 1978). We used this fact to calibrate between the Fe XI and Fe XIV continuum data from Mitchell, where the off-band observations were free of Doppler contamination. The solar disk ND filter observations already calibrated each on- and off- band pair. However, to calibrate the Fe XI and Fe XIV to each other, we took the average intensity ratio of the continuum data below 1.1 $R_\odot$ in a 30° region centered on the western streamer. In doing so, we created a map of the F corona red excess (see Appendix A), and provided the final step in the cross calibration between all datasets at Mitchell (i.e., $\frac{\rho(\nu_k)\ \epsilon_k}{\rho(\nu_j)\ \epsilon_j}$ in Equation (9), Section 3.2.3).

The Fe XI continuum data is then modeled for Mackay and Alliance by taking the reddening correction for the F corona observed at Mitchell, and applying it to the calibrated Fe XIV and Ar X continuum data from Mackay and Alliance, respectively. This technique provides the shape of the continuum for Fe XI at Mackay and Alliance, but does not provide an intensity calibration. Given that the Mitchell data was pristine, we calibrated the line data (i.e., on—continuum) for Mackay and Alliance using the average line to continuum ratio found in the north coronal hole (<1.1 $R_\odot$) of the Mitchell data. This procedure assumes that the Fe XI line to continuum ratio in the coronal hole did not change over the 28 minutes between sites, which may not be the case. Nonetheless, this calibration provides a means for setting the lower limit on the size of changes during this time. If the coronal hole also changed, then the magnitude of changes (both T_e and Fe XI line to continuum ratio) presented in this work would only increase. Additionally, the F corona intensity is exceptionally constant throughout the solar cycle (Morgan & Habbal 2007), so any inferred changes between sites (see Sections 3.1 and 4.2) cannot be due to the F corona.

2.3. Spacecraft Observations

A series of eruptive events occurred in the corona just prior to the time of the eclipse, as illustrated by *SDO*/AIA and *Solar*

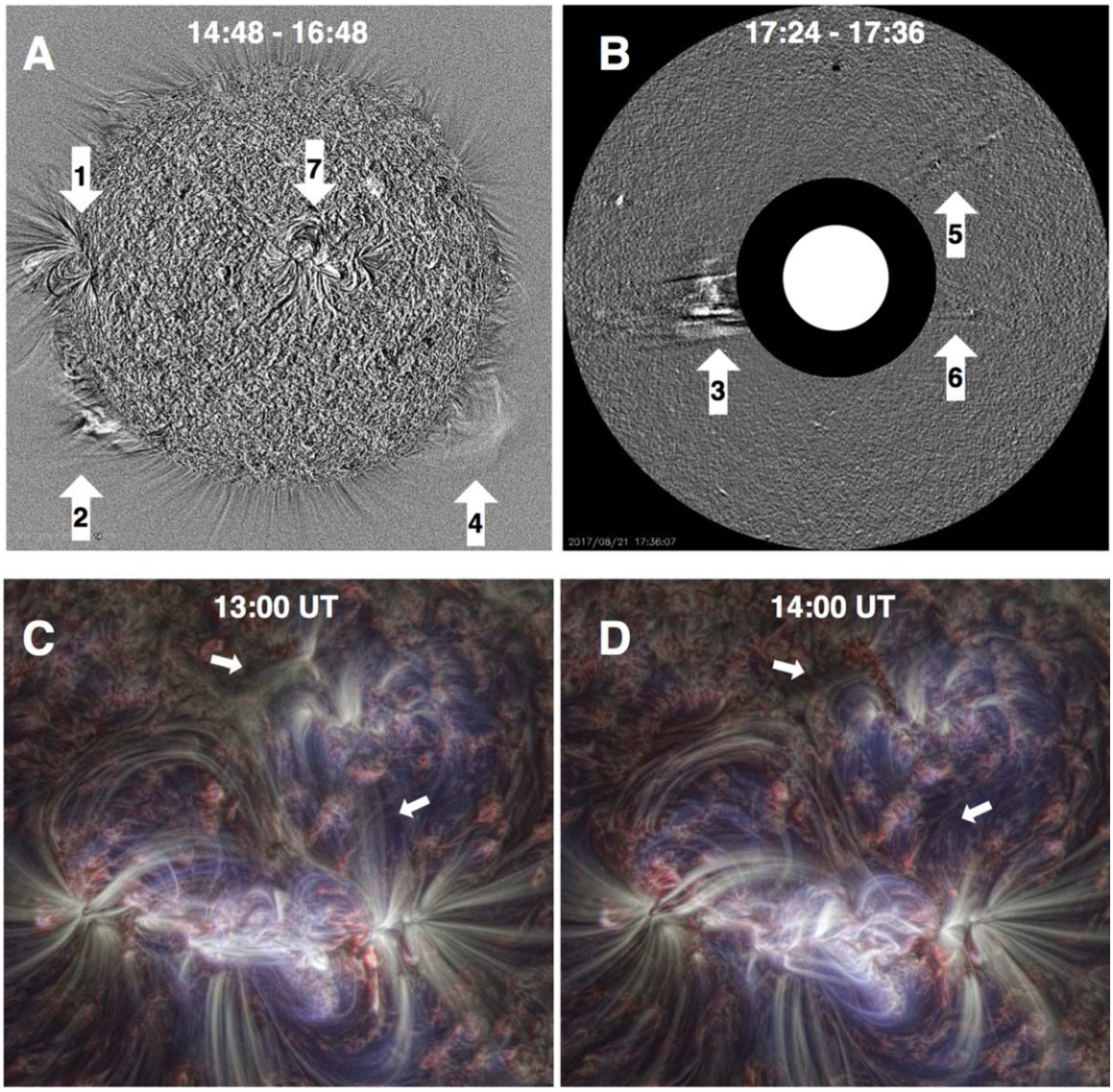

Figure 2. A: Difference between two processed *SDO*/AIA 17.1 nm images showing changes over two hours prior to the eclipse (14:48 and 16:48 UT), with arrows indicating active region 12672 (arrow 1) and 12671 (arrow 7) along with some erupting structures that will impact the outer corona, namely a joint eruption of active region 12672 (arrow 1) and a prominence in the southeastern corona (arrow 2). B: Difference between two processed *SOHO*/LASCO-C2 images from 17:24 and 17:36 UT, showing eruptions (arrows 3, 5 and 6) in the corona occurring at the time of the eclipse. The inner white circle represents the approximate size of the solar disk. C and D: PM-NAFE processed AIA data of the disk center active region (12671) at 13:00 and 14:00 UT, respectively. The arrows indicate changes in the PM-NAFE maps, likely due to a halo-CME erupting from this active region (see Section 2.3 for details on the image processing). An animation of panels "c" and "d" is available. The video begins on 2017 August 21st 12:00:05 and ends the same day at 14:59:41. The realtime duration of the video is 36 s.

(An animation of this figure is available.)

and Heliospheric Observatory (*SOHO*)/LASCO spacecraft observations presented in Figures 2–4. Figure 2(A) shows the difference of two AIA 17.1 nm images processed using the Multi-scale Gaussian Normalization technique (MGN) from Morgan & Druckmüller (2014) just prior to the eclipse (at 14:48 and 16:48 UT). Panel (B) shows a differenced LASCO-C2 image (at 17:24 and 17:36 UT) that was processed using the Dynamic Separation Technique (DST) from Morgan et al. (2012), Morgan (2015). Panels (C) and (D) show PM-NAFE (Planckian Mapping-Noise Adaptive Fuzzy Equalization) processed AIA data of the disk center active region (AR 12671). PM-NAFE is an algorithm developed by Druckmüller (2013) to combine *SDO*/AIA data into a single composite image, where the color of the image corresponds to the average electron temperature inferred by the relative flux of the AIA channels. A video covering several hours of the full disk PM-NAFE processed data around the time of the CMEs is available in the online version of the article. Figure 3 contains a series of difference images for the same disk center active region that were created by directly subtracting pairs of two AIA images, so they indicate changes in the absolute EUV emission within the bandpass. This technique is different from the panels in Figure 2, which were first processed with MGN, DST, or PM-NAFE to enhance structural features. Figure 4 shows the time evolution of the continuum corona as seen by LASCO-C2, including a transient spike in continuum emission that occurred around the time period between Mackay and Alliance. The bottom of Figure 4 also contains in situ alpha particle abundance data from the *ACE* spacecraft (Stone et al. 1998) for several days after the eclipse.

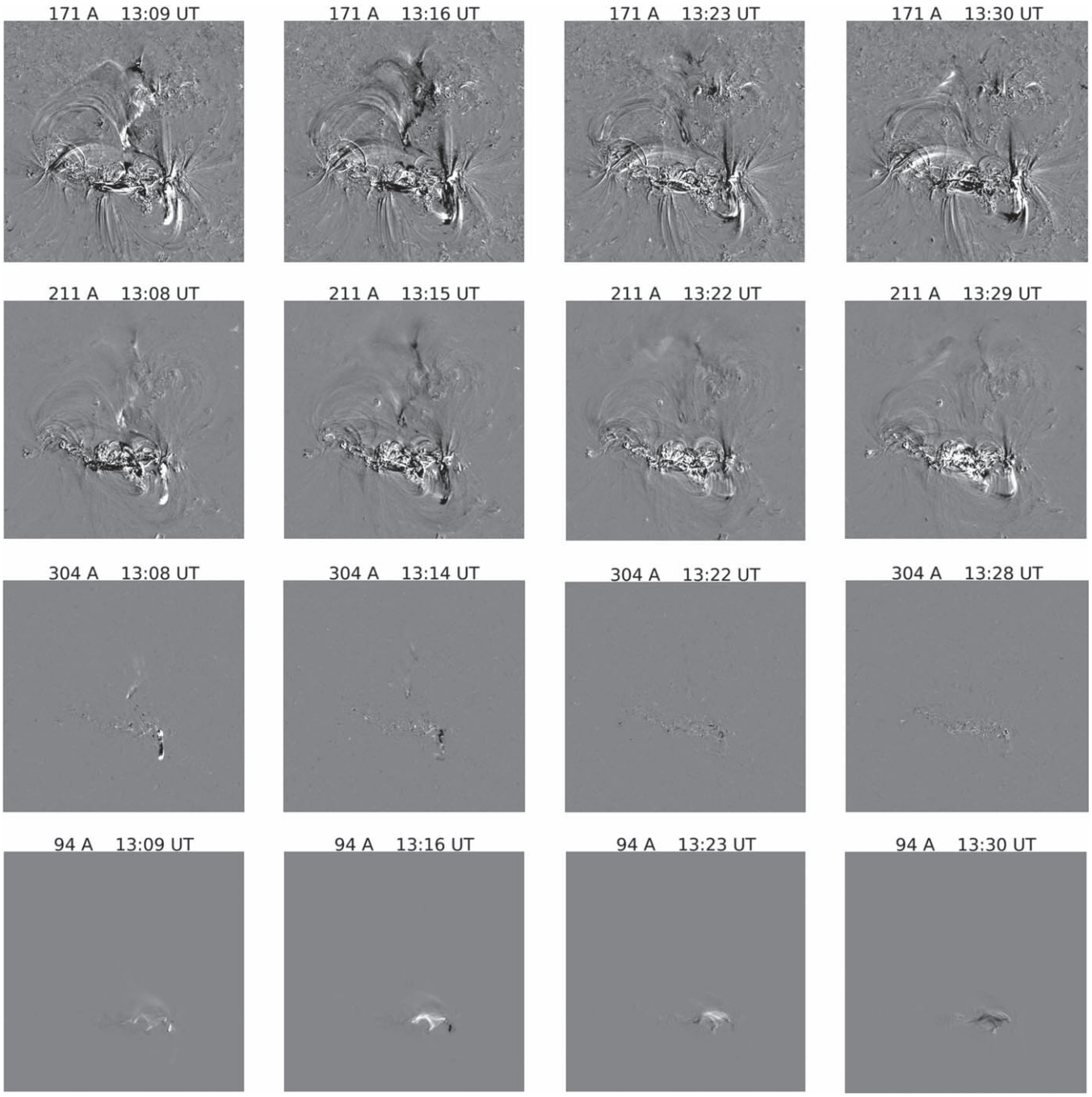

Figure 3. Absolute difference images of *SDO*/AIA centered on active region 12671 (see arrow 7 in Figure 2), which was near disk center and 10° north latitude at the time of the eclipse. Each frame shows the change over a ≈7 minute period. From top to bottom, the rows show emission changes from 17.1 nm (Fe IX), 21.1 nm (Fe XIV), 30.4 nm (He II), and 9.4 nm (Fe XVIII). These changes highlight a CME that occurred almost simultaneously with other eruptive events near the limb of the corona (see Figure 2).

The most notable event recorded by the spacecraft observations prior to the eclipse was a CME that erupted from active region 12672 on the east limb (arrow 1 in Figure 2(A)) coupled with a filament eruption to the south (arrow 2 in Figure 2(A)). Around approximately 13:00 UT on the day of the eclipse, the CME and faint prominence core began moving slowly outward, as seen in the AIA images. By 16:00 UT, the CME had moved out of the AIA field of view (≈1.2 $R_{\odot}$). The CME was first visible by LASCO-C2 on *SOHO* (≈2.0$R_{\odot}$, see arrow 3 in Figure 2(B)) by 17:00 UT until at least 22:00 UT (the first eclipse in our dataset began at 17:21). During the time interval of the eclipse observations at all three sites, the CME front had made its way toward the edge of our images (≈2–3 $R_{\odot}$), having disturbed the lower corona over the preceding few hours. There were two other small eruptive like regions in the north- and south-western corona (see arrows 4, 5 and 6 in Figure 2) that are noticeable in the AIA 17.1 nm and LASCO-C2 differenced images. These smaller eruptions do not necessarily generate a CME (i.e., an eruption that fully escapes from the Sun), but they can still have an impact on the thermodynamics in the corona (as shown in Sections 3.1, 3.2.3, and 4.2).

At the same time that the eruptions near the limb of the Sun began, there were motions occurring in active region 12671

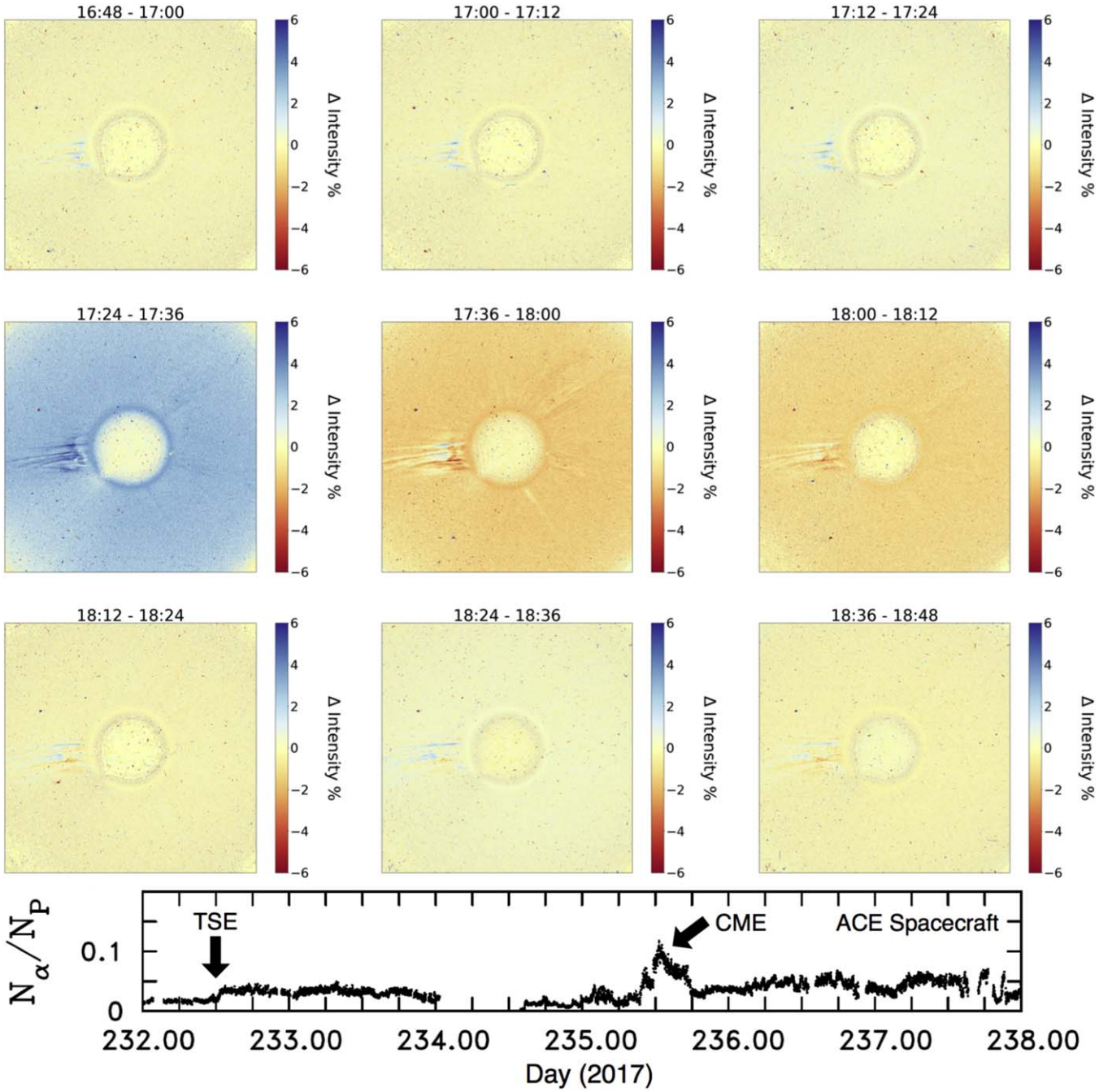

Figure 4. Top: Percentage difference images of LASCO-C2 coronagraph data indicating the total white light continuum intensity changes around the time of the eclipse. There is a substantial increase in emission (>3%) occurring between 17:24 and 17:36, which roughly coincides with the times of totality at Mitchell and Mackay. The increase, and subsequent decrease in emission, is evidence of halo-CME activity during the period of eclipse observations. Bottom: Alpha particle abundance relative to protons in the solar wind at L1 as observed by the *ACE* spacecraft. Arrows indicate the time of the total solar eclipse (TSE) and the signature of a CME arriving about 3 days after the eclipse.

(see C and D in Figures 2, and 3) that appear to be a CME event near the center of the solar disk. Around 13:00 UT on the day of the eclipse, outward motions and the following disappearance of closed field lines on the north side of the active region are seen by the 17.1 (Fe IX) and 21.1 nm (Fe XIV) channels, while the chromosphere (30.4 nm, He II) and high temperature plasma (9.4 nm, Fe XVIII) show a short duration spike in flare-like emission that is characteristic of the base of an erupting CME from an active region (e.g., Fletcher et al. 2011 and references therein). Given the location of the active region, the CME is likely to be moving almost directly toward the Earth, perhaps slightly northward given the latitude of the active region. Structural variation in the corona caused by such a relatively small halo-CME would be exceedingly difficult to detect in the LASCO-C2 coronagraph data, but the continuum intensity variation is detectable. The LASCO-C2 coronagraph data show a transient increase in white light emission occurring during the period of the eclipse (see Figure 4), which is likely caused by this halo-CME. The *ACE* spacecraft (Stone et al. 1998) at the L1 Lagrange point also observed a transient spike in the alpha particle abundance (He abundance is an indicator of interplanetary CMEs; e.g., Borrini et al. 1982). The

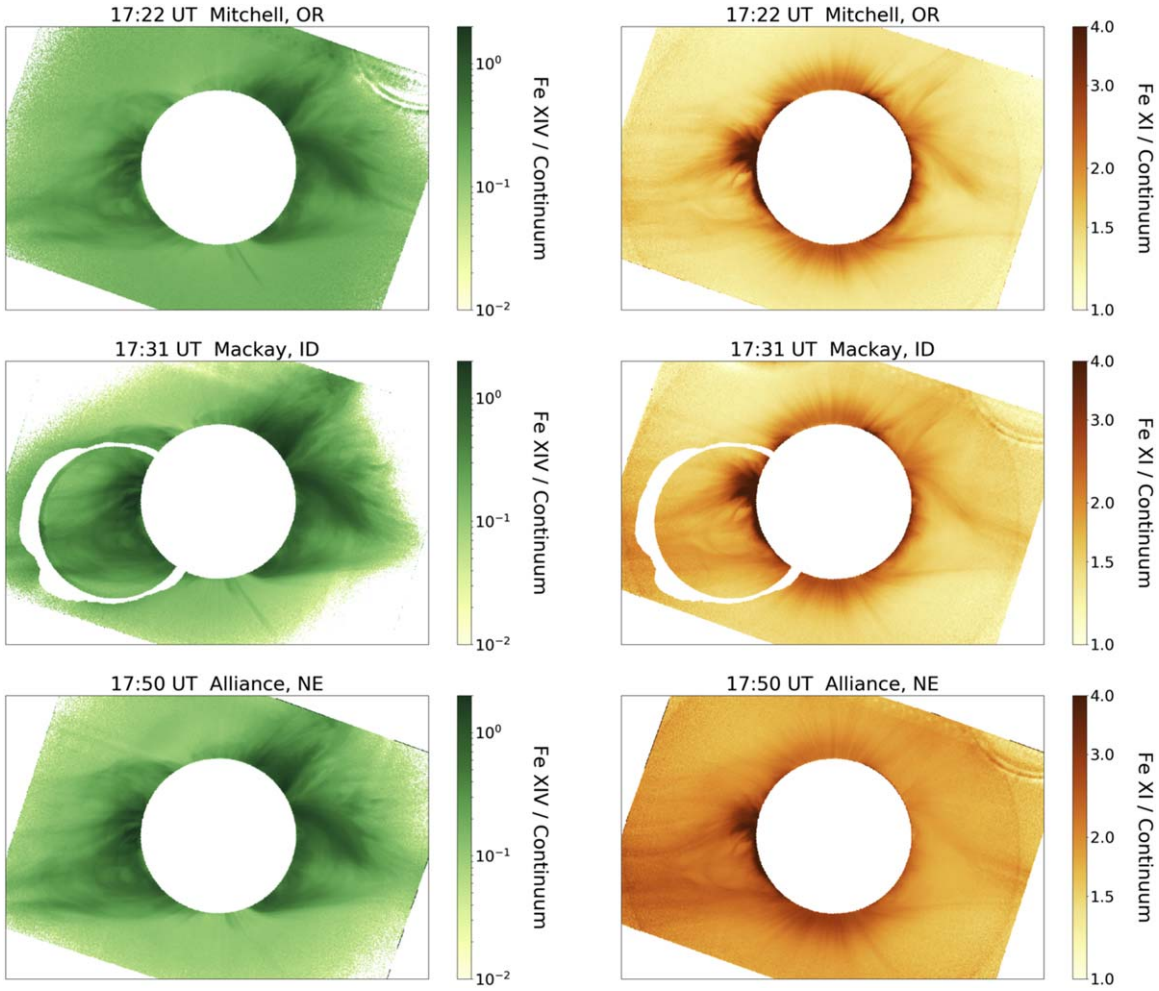

Figure 5. Line to continuum ratio of Fe XIV (left) and Fe XI (right) made at three separate sites (see Section 3.1). The line and continuum data were calibrated using the technique outlined in Section 2.2. The white ring in the middle panels indicates the location of a ghost image in the raw data that was produced by internal reflections in the optics (see Appendix B).

alpha particle abundance was initially stable around ≈3% of the proton density for several days, then the abundance rose to between 5% and 10% for several hours about three days after the eclipse (see bottom of Figure 4). The time delay would correspond to ≈545 km s^{-1} assuming the CME traveled at a constant velocity after eruption at 13:00 UT on the day of the eclipse. The presence of a halo-CME is further supported by changes in Doppler emission of Fe XI (see Appendix A). The simultaneity of these two CMEs and sub-eruptive events in the streamers hint that there was some magnetic connectivity between these regions leading to "sympathetic CME" behavior (i.e., Moon et al. 2003). It is likely that these events caused global scale perturbations in the corona (see Sections 3.2.3, and 4.2).

3. Observational Metrics

3.1. Line to Continuum Ratio

Observations of the Fe XI and Fe XIV line emission (see Section 2.1) were calibrated relative to continuum emission observations (see Section 2.2), which enabled the measurement of ionic emission normalized by the continuum emission from 1 to 3 $R_{\odot}$, as shown in Figure 5. Identical observations were made at three separate observing sites, which enabled the quantification of changes of the line to continuum intensity ratio over the 28 minutes between the time of totality at the first and last site as shown in Figures 6 and 7. We only display those regions of the maps that had a signal to noise ratio >5 (from photometric and calibration uncertainties, see Section 2.2) in the narrowband images used for each plot.

The dynamics of the line to continuum observations are complex to analyze because they will change as a result of temperature, density and velocity effects. Since we are observing the line emission with very narrowband filters (≈0.5 nm width), any plasma with a radial velocity (RV) faster than ≈190 km s^{-1} for Fe XI and ≈280 km s^{-1} for Fe XIV will be Doppler shifted out of our line emission observations (i.e., shifted out of the filter bandpass). This velocity shift will not change the continuum emission from the K+F corona because it is re-emitting a broad continuum spectrum from the photosphere. Consequently, the continuum intensity is integrated along a large three-dimensional column along the line of sight in contrast to the line emission observation, which will only observe coronal plasma near the plane of the sky with little to no Doppler velocity. Therefore, the line to continuum measurements indicate the total line emission of particles with no RV relative to the global line of sight corona continuum.

As shown in Figure 5, the ionic emission relative to the continuum spans about 3 orders of magnitude in the corona for

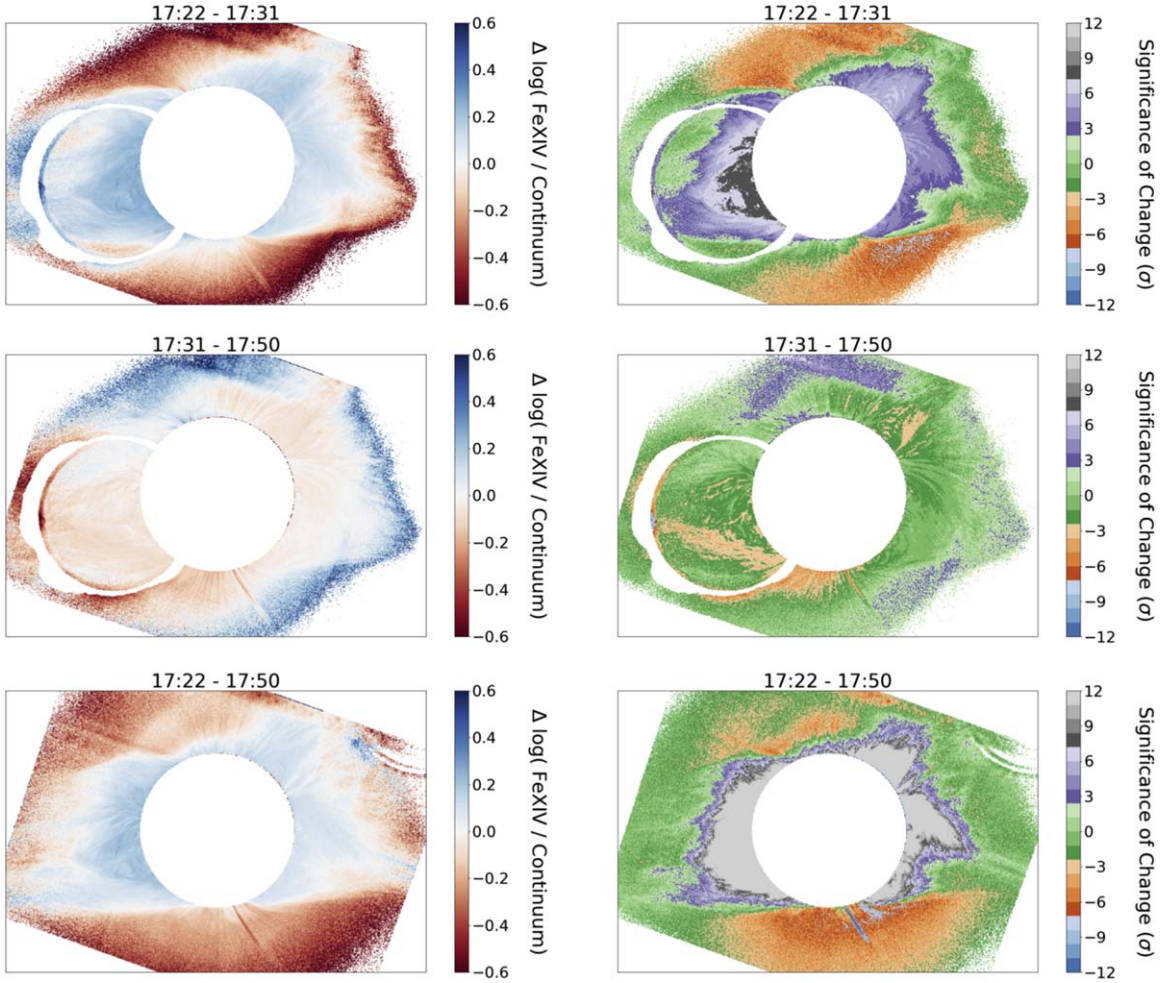

Figure 6. Left: Change in the Log_{10} of the Fe XIV line to continuum ratio between the three observing sites (see Sections 3.1 and 4.2). Right: Statistical significance of these changes between sites. Top: Mackay–Mitchell; Middle: Alliance–Mackay; Bottom: Alliance–Mitchell. The white rings in the top and middle panels are the same indication of a ghost image as in Figure 5.

Fe XIV, while Fe XI emission is confined to less than a single order of magnitude of intensity variation in the corona. Streamer regions have the highest Fe XIV emission, typically staying around the same intensity as the continuum. In the coronal holes, Fe XIV is far less abundant, going down to around 1% that of the continuum. The Fe XI emission is stronger than the continuum emission throughout the entire corona, and is strongest in the western limb active region (see Section 2.3), where it is as much as six times the continuum intensity (note that the scale in Figure 5 is limited to provide contrast for lower intensity regions). The strong emission of Fe XI around the active region supports the idea of open field regions in the vicinity of active regions, as previously suggested by Sakao et al. (2007) and Harra et al. (2008).

The low intensity of Fe XIV relative to the local continuum is quite a bit lower than what is predicted by Bemporad et al. (2017), who argue that a single observation of the Fe XIV emission without a continuum subtraction can give useful results. In fact, we find that the "spectral purity" of Fe XIV is less than 50% in our 0.5 nm bandpasses almost everywhere in the corona, which is more similar to the spectral purity that Bemporad et al. (2017) predicts for a 1 or 2 nm bandpass. Observation and subtraction of the continuum subtraction is absolutely essential to infer any physical properties of the corona other than morphological structure (see Section 2.1). Furthermore, inferring physical properties with an on-band Fe XIV data alone is inherently biased and should not be trusted.

The time variations between observing sites are shown for Fe XIV (Figure 6) and Fe XI (Figure 7) with time changes of 9 (site 1–2), 19 (site 2–3) and 28 (site 1–3) minutes, respectively. Statistically significant changes for both ions occurred between the sites, as demonstrated by the right-hand panels in both figures, which indicate the statistical significance of the changes based on the error from both line to continuum measurements.

The general behavior of the line to continuum ratio indicates that both the line of sight temperature and density distributions were changing globally in the corona. These changes are likely to be caused by the CME events that occurred prior to the eclipse, as described in Sections 2.3, and 4.2. During the 9 minute period between Mitchell, OR, and Mackay, ID, the Fe XIV line to continuum ratio is increasing in the low corona, and decreasing in and around the coronal holes. Over the next 19 minutes from Mackay, ID, to Alliance, NE, the Fe XIV emission decreases at the site of the CME, while it is increasing slightly in the outer coronal holes. The net effect over the entire 28 minutes between Mitchell, OR and Alliance, NE is a large

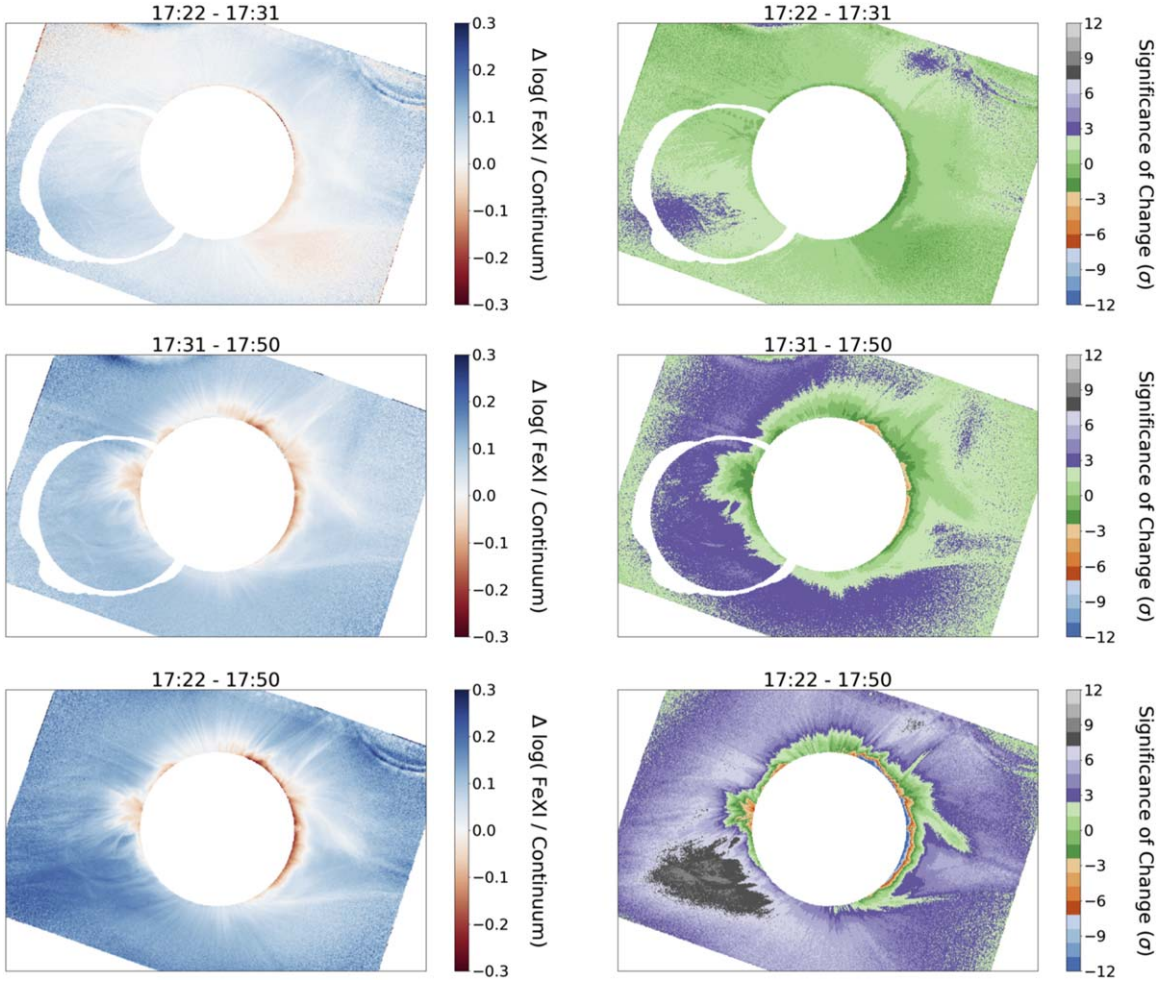

Figure 7. Left: Change in the Log_{10} of the Fe XI line to continuum ratio between the three observing sites (see Section 3.1 and 4.2). Right: Statistical significance of these changes between sites. Top: Mackay–Mitchell; Middle: Alliance–Mackay; Bottom: Alliance–Mitchell. The white rings in the top and middle panels are the same indication of a ghost image as in Figure 5.

decrease in Fe XIV emission in the coronal holes with a modest increase (still highly statistically significant) in the streamers below $\approx 2R_{\odot}$. The Fe XI line to continuum ratio was growing throughout the corona, with the largest increase centered on the location of the western CME (see Section 2.3). It is important to note that the Mackay and Alliance Fe XI line to continuum ratio had to be normalized to the pristine Mitchell data in the north polar hole ($<1.1\,R_{\odot}$) because of some calibration issues (see Section 2.2), so the increase is relative to the line to continuum ratio in the north polar hole. If line of sight effects from the CME also increased Fe XI emission around the coronal hole, then the changes between sites would be even larger than what we have reported.

3.2. Electron Temperature Inference

The line to continuum observational metric presented in Section 3.1 is useful for inferring some physical properties of the coronal plasma. However, it is difficult to interpret because it can be altered by density, temperature and velocity effects. To investigate the thermodynamic properties of the solar corona, we used all Fe XI and Fe XIV imaging data to infer the relative abundance of Fe^{10+} and Fe^{13+} throughout the corona and to calculate an electron temperature corresponding to the ionic abundance ratio. A description of the method used to make this inference follows.

3.2.1. Emission Rules

Spontaneous line emission causes the transition of an atom from an excited state (with density n_u) to a lower state (with density n_l). The rate of emission per unit time can be written as:

$$A_{ul}\ n_u, \tag{2}$$

where A_{ul} is the Einstein coefficient for radiation from a given excited state of the atom.

Similar to emission, the rate of photon absorption is described by:

$$B_{lu}\ n_l\ \rho(\nu), \tag{3}$$

where B_{lu} is the Einstein coefficient for absorption and $\rho(\nu)$ is the energy density at the same frequency as the given atomic transition (units of $\mathrm{J\,m^{-3}\,Hz^{-1}}$). The relationship between the Einstein coefficients is given by:

$$A_{ul} = B_{lu}\frac{g_u}{g_l}\frac{8\pi h\nu^3}{c^3}, \tag{4}$$

with g_u and g_l being the statistical weights of the excited and lower states, respectively (Herzberg 1945).

Since we are interested in the total abundance of an ion regardless of its excitation state, we must account for the ion's electronic state distribution. In thermodynamic equilibrium, this can be done simply with the Boltzmann formula, although it is not applicable in the low density environment of the corona. In the absence of collisional effects, the level distribution of an ion will depend on the relative rates of radiative absorption spontaneous decay alone (i.e., Equations (2) and (3)).

It is possible that non-equilibrium collisional effects could change the level population, but these effects should be unimportant everywhere except in the very low corona. Habbal et al. (2007) showed that the Fe XI and Fe XIV emission lines specifically will be excited much more frequently by radiative absorption than by collisions, even for densities as high as $n_e = 2 \times 10^7\,\mathrm{cm}^{-3}$. In the very low corona (below $\approx 1.2\,R_\odot$), collisional effects may become comparable with radiative effects and slightly bias our inferred ionic density ratio if the density is higher than $\approx 10^7\,\mathrm{cm}^{-3}$. Our results should therefore only be considered robust for distances larger than about $1.2\,R_\odot$ (given the density profile for a coronal hole from Cranmer et al. 2007). Streamers will have a higher density, so the distance where collisions are important could be farther away from the Sun in this case. Nevertheless, collisions will increase the emission of *both* Fe XI and Fe XIV at a rate proportional to the density squared, and so the line emission ratio should not change substantially due to collisions.

If there is a high enough energy density of incoming photons, it is possible that some fraction of the ionic density may become trapped at a higher electronic state, which would affect the value of n_u, n_l, and other possible electronic states. What follows is a short proof that the rate of spontaneous decay is in fact far greater than that of radiative absorption for any arbitrary choice of coronal ionic emission line.

3.2.2. Level Population Proof

Measurements from the International Space Station (ISS) show that the solar spectral energy density at 1 au has a maximum of about $2\ \mathrm{J\ s^{-1}\ m^{-2}\ nm^{-1}}$ at approximately 550 nm (see the top panel in Figure 8, Meftah et al. 2018), corresponding to about $2 \times 10^{-12}\ \mathrm{J\ s^{-1}\ m^{-2}\ Hz^{-1}}$. Treating the Sun as a point source results in an intensity of solar photons in the corona (say at the photosphere $R = R_\odot$) of $\approx 10^{-7}\ \mathrm{J\ s^{-1}\ m^{-2}\ Hz^{-1}}$. Converting this to an energy density (dividing by the speed of light) gives $\rho(\nu) \approx 3 \times 10^{-16}\ \mathrm{J\ m^{-3}\ Hz^{-1}}$ for the photon energy density in the corona at 550 nm. Multiplying $\rho(\nu)$ by B_{12} (substituting with Equation (4)) gives:

$$\rho(\nu) \times B_{lu} = \ 3 \times 10^{-16}\, A_{ul}\, \frac{g_u}{g_l} \frac{c^3}{8\pi h \nu^3} \ \approx 0.003 \times A_{ul}, \tag{5}$$

provided that the statistical weights are the same within an order of magnitude (since the g's are known for a given line, this proof applies to any arbitrary line). Equation (5) indicates that the rate of spontaneous decay is about 10^3 times higher than the rate of resonance excitation for ions in the corona at around 550 nm. This same calculation was repeated for the entire solar spectrum in the vicinity of visible wavelengths, as shown in Figure 8. These calculations indicate that the rate of resonant excitation from photospheric photons will be at least two orders of magnitude lower than the rate of spontaneous decay of the same state for every possible electronic level transition with wavelengths ranging from the EUV to the near-infrared. The radiation density provided by the solar photosphere is simply not high enough to cause resonance excitation at a fast enough rate to substantially populate any state other than the lowest level.

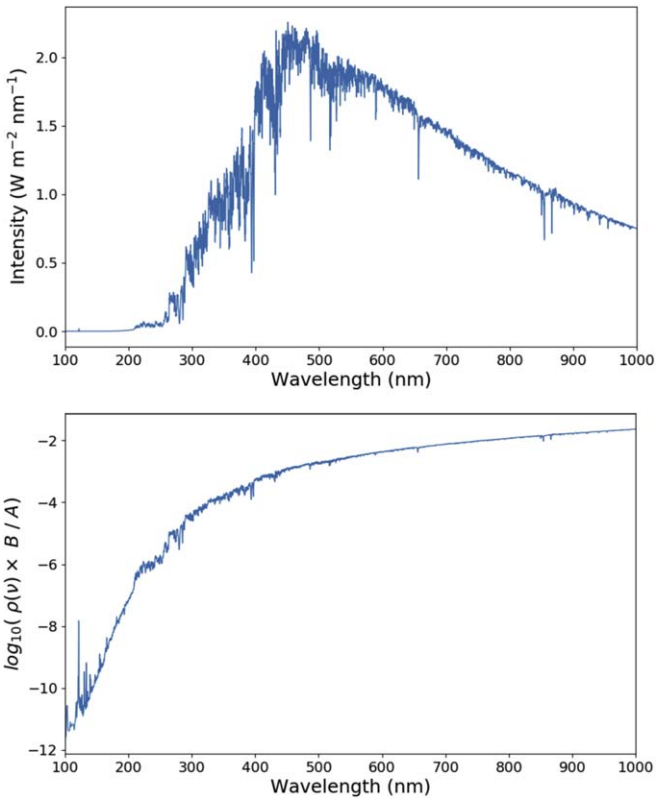

Figure 8. Top: Solar spectral energy density from ISS observations at 1 au (Meftah et al. 2018). Bottom: Relative rate of photoexcitation and spontaneous emission vs. wavelength for any energy level transition based on the energy density from the top curve (scaled to $1\,R_\odot$) as shown in the example in Section 3.2.2. For all visible (and shorter) wavelengths, the rate of spontaneous emission is at least 2 orders of magnitude smaller than photoexcitation.

3.2.3. Electron Temperature

The example from Section 3.2.2 (see Figure 8) demonstrates that for typical coronal conditions (i.e., $n_e < \approx 10^7\,\mathrm{cm}^{-3}$), one can assume that all ions are in the ground electronic state, except for rare instances when they absorb photons and immediately decay spontaneously. Thus, $A_{ul} \gg B_{lu} \times \rho(\nu)$ and the density of the excited state, n_u, will be quickly depleted to the ground state, n_l, for all possible energy states. This depletion of higher states will cause the total density of the ion, n_i, to be about equal to the density in the ground state ($n_i \approx n_l$). Therefore, every emitted photon from the coronal ions will originate from a very recent photoabsorption, and the total number of photons emitted per unit time will be given by Equation (3) for any coronal ion emission line that ends in the ground state.

The intensity in our eclipse images (see Section 2.1) for the on-band, $I_{\mathrm{on},i}$, and the continuum $I_{\mathrm{cont},i}$, can be related by:

$$I_{\mathrm{on},i} - I_{\mathrm{cont},i} = B_{lu,i}\ \rho(\nu_i)\ n_i\ \epsilon_i, \tag{6}$$

where ϵ_i is the efficiency of the photometric observations (after calibration, see Section 2.2).

Table 2
Constants Used for Equation (9)

Line	λ_{ion} (nm)	ν_{ion} (10^{14} Hz)	A_{ion} (s^{-1})	g_l	g_u
Fe XI	789.2	3.801	43.7	5	3
Fe XIV	530.3	5.657	60.2	2	4

Note. Data from NIST (Kramida et al. 2018 and references therein).

Now consider two different ionization states j and k (analogous to Fe^{10+} and Fe^{13+}) and take the ratio of Equation (6) for j and k,

$$\frac{I_{on,j} - I_{cont,j}}{I_{on,k} - I_{cont,k}} = \frac{B_j\ \rho(\nu_j)\ n_j\ \epsilon_j}{B_k\ \rho(\nu_k)\ n_k\ \epsilon_k}. \quad (7)$$

Substituting B_j and B_k from Equation (4) gives,

$$\frac{I_{on,j} - I_{cont,j}}{I_{on,k} - I_{cont,k}} = \frac{\rho(\nu_j)\ n_j\ \epsilon_j\ A_j\ g_{u,j}\ g_{l,k}\ (\nu_j)^{-3}}{\rho(\nu_k)\ n_k\ \epsilon_k\ A_k\ g_{l,j}\ g_{u,k}\ (\nu_k)^{-3}}. \quad (8)$$

Finally solving for the density ratio gives:

$$\frac{n_j}{n_k} = \frac{(I_{on,j} - I_{cont,j})\ \rho(\nu_k)\ \epsilon_k\ A_k\ g_{l,j}\ g_{u,k}\ {\nu_k}^3}{(I_{on,k} - I_{cont,k})\ \rho(\nu_j)\ \epsilon_j\ A_j\ g_{u,j}\ g_{l,k}\ {\nu_j}^3}, \quad (9)$$

where $\frac{\rho(\nu_k)\ \epsilon_k}{\rho(\nu_j)\ \epsilon_j}$ is measured as the continuum ratio in the low corona between the continuum datasets for each line after the on- and off-band pairs were self-calibrated with solar disk observations (see Section 2.2 for details).

Equation (9) provides a method for using four different imaging observations, namely a continuum observation combined with the on-band observations of two different optical forbidden emission lines of the same element (with a relative calibration), to directly calculate the relative density of two ions. We computed Equation (9) separately for every line of sight to measure the relative density of Fe^{10+} and Fe^{13+} throughout the corona at each site. The constants used in this calculation are shown in Table 2. The relative density maps are then used to infer the electron temperature based on the results of Arnaud & Raymond (1992), who calculated the ionization equilibrium abundances as a function of T_e for many states of Fe (see Figure 9). The Arnaud & Raymond (1992) abundance values were calculated in steps of $\Delta\mathrm{Log}(T_e) = 0.1$; we have interpolated their data for this work.

Arnaud & Raymond (1992) used a low density approximation where "the steady state ionic fractions do not depend on electron density," which is the same assumption that we make in our analysis. The Arnaud & Raymond (1992) results also assume ionization equilibrium, which is not necessarily valid beyond $\approx 1.5 R_\odot$ (see Section 1; Landi et al. 2012). We will not consider non-equilibrium effects here, but rather report on the inferred T_e based on the relative ion density alone (inferred from emission assuming no collisional effects), which is then directly comparable with inferred coronal T_e values from in situ ionic charge state measurements. We chose to use the Arnaud & Raymond (1992) abundances due to the lack of dependence on free parameters. A more complex model to measure the true kinetic electron temperature would require constraints on the density and outflow velocity, which were not possible to measure directly with our data and would induce additional uncertainty into the results. In addition, our observations do not measure T_e for a single isothermal unit of plasma, but rather we measure the line of sight average emission of Fe XI and Fe XIV. Therefore, our inferred T_e values provide a density weighted average of the electron temperature distribution near the plane of the sky.

It is also important to remember that once the plasma reaches the freeze-in distance ≈ 1.2–$1.4 R_\odot$ for coronal holes and up to 1.6–$1.8 R_\odot$ for streamers, as shown by Boe et al. (2018), the ionic abundance (and so the inferred T_e) will remain constant as the plasma flows outward in the solar wind. Beyond the freeze-in distance, our inferred T_e will be representative of what the T_e was in the low corona when the plasma was below the freeze-in distance. In fact, the ionic abundances may decouple from T_e even below the freeze-in distance as shown by Landi et al. (2012).

The inferred Fe^{13+} to Fe^{10+} ionic density ratio and corresponding T_e are shown in Figure 10. The density ratio maps show that the coronal holes at the north and south poles have a Fe^{13+} density that is about 2%–5% of the Fe^{10+} density. Meanwhile, the streamers contain a much larger amount of Fe^{13+}, which ranges from 10% to 50% of the Fe^{10+} density. Overall, the ionic density ratio varies by over an order of magnitude in the corona. The inferred T_e in coronal holes is the lowest, about $(1.1$–$1.2) \times 10^6$ K, whereas streamers have the highest temperatures, ranging from 1.2 to 1.4×10^6 K. The coronal regions that have the highest T_e correlate well with the presence of closed magnetic field lines, underlying prominences (as shown previously by Habbal et al. 2010a), and a high continuum intensity (i.e., high electron density).

The coronal T_e changed significantly along most lines of sight between the sites, as shown in Figure 11, with the largest change occurring between the first and last site. The outer regions of the corona are found to be cooling with time while the inner regions are heating up. Many of these changes are significant to greater than 3σ, with the lower regions of streamers commonly changing by $>10\sigma$ based on propagated calibration and $\sqrt{N}$ photometric errors (where N is the number of data counts in the original images, see Section 2.1). A discussion on the nature of these changes is given in detail in Section 4.2.

4. Discussion

4.1. Spatial Distribution of T_e

Inferences of the coronal electron temperature (T_e) throughout the corona (see Figure 10) indicate that each individual field line has a unique temperature structure. The large variability in T_e in streamer regions implies the existence of a preponderance of structures in the corona, each with unique temperature and density profiles depending on the exact physical parameters that act upon the field line. A physically realistic coronal heating model should be able to explain the diversity of temperature conditions that are present along various field lines.

The coronal holes have inferred T_e's between 1.1 and 1.2×10^6 K, which is in agreement with previous UV and EUV emission measurements that yielded coronal hole temperatures in the range of $(1.1$–$1.3) \times 10^6$ K (Habbal et al. 1993; Dudok de Wit et al. 2013), albeit in the very low corona ($<1.2\,R_\odot$). The same temperature range for polar coronal holes was also inferred at large heliocentric distances using charge state measurements over multiple solar cycles by the *Ulysses* and *ACE* spacecraft (Smith et al. 2003; Habbal et al. 2010b). The consistency of the inferred coronal hole temperatures,

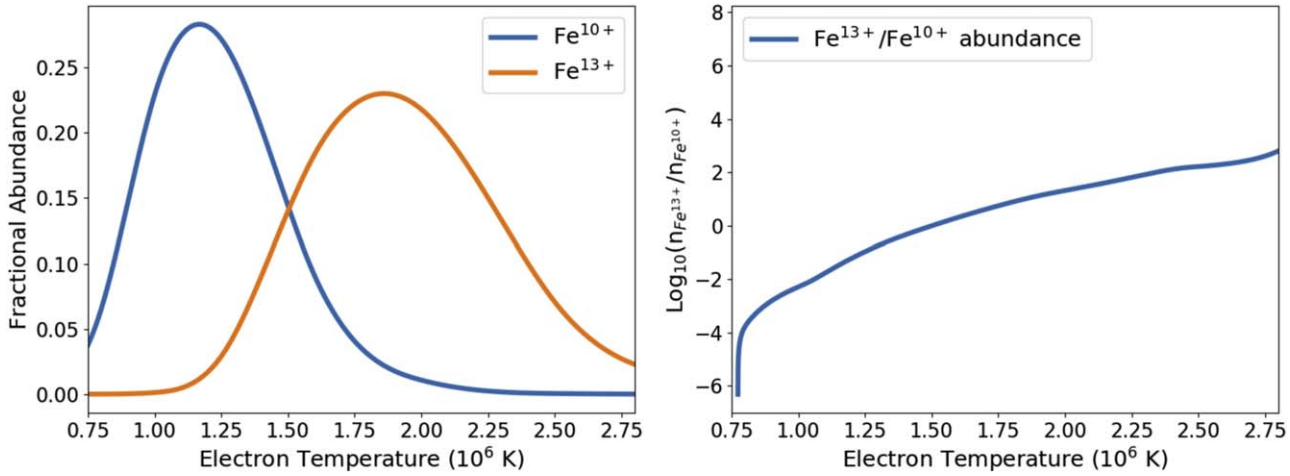

Figure 9. Temperature dependence of the fractional ionic abundance of Fe $^{10+}$ and Fe $^{13+}$ interpolated from the calculations of Arnaud & Raymond (1992) (left) and of the abundance ratio (right).

using vastly different techniques across multiple solar cycles, hints that coronal heating mechanisms within open magnetic field line regions are relatively stable throughout multiple cycles.

The inferred T_e values in streamers and closed field line regions range from 1.2 to 1.4 $\times$ 10^6 K. These T_e values are consistent with the quiet Sun regions inferred by *SDO*/AIA below 1.2 $R_\odot$, but are far lower than the typical active region temperatures of (2–4) $\times$ 10^6 K (e.g., Dudok de Wit et al. 2013; Morgan & Taroyan 2017). This difference is likely caused by observational selection effects that are very different in optical versus EUV observations. The solar photosphere emits very little in the EUV (see Figure 8), so the rate of radiative excitation for EUV lines is much smaller than for optical lines. Coronal EUV emission is consequently dominant where it is collisionally excited ($\propto n_e^2$) in the low corona and closed field line regions ($<$1.2 $R_\odot$), while optical emission lines will originate from radiatively excited plasma ($\propto n_e$) on both open and closed field lines near the plane of the sky, out to at least 2–3 $R_\odot$. It is reasonable to expect that observations of different sets of emission lines that operate with different non-equilibrium excitation mechanisms will result in a different temperature inference. Regardless, our metric for inferring the electron temperature is self-consistent and is useful for inferring dynamic and thermodynamic changes in the corona, even if it is not an exact kinetic electron temperature for a single isothermal plasma element.

Another key difference between the work presented here and T_e studies using *SDO*/AIA data is the temperature response of the observed emission lines. We used emissions from Fe^{10+} and Fe^{13+}, which will be sensitive to plasma with temperatures between about 1 and 2 $\times$ 10^6 K (see Figure 9). Any plasma at a higher or lower temperature than that range will not be visible in our observations. *SDO*/AIA has bandpasses that are sensitive to T_e as high as 10^7 K, and so they are capable of measuring higher T_e plasma (e.g., O'Dwyer et al. 2010; Boerner et al. 2012; Morgan & Taroyan 2017). Data in situ from *Ulysses* and *ACE* over multiple solar cycles indicates that the average coronal T_e is around (1.2–1.5) $\times$ 10^6 K (McComas et al. 1998; Gloeckler et al. 1998; Smith et al. 2003), while there are still occasional short duration spikes in T_e that can go as high as 10^7 K (e.g., Habbal et al. 2010b). Combining in situ and emission line observations leads to the interpretation that the vast majority of the plasma in the corona is $<$1.5 $\times$ 10^6 K, except for some higher T_e plasma originating from closed field lines in and around active regions. Some of this hotter plasma can be released via CMEs and reconnection events into the solar wind, but it will only compose a small fraction of the total solar wind plasma.

4.2. Thermodynamic Temporal Variability

As noted earlier in Section 3.1, there were significant changes in the Fe XI and Fe XIV emission relative to the continuum (see Figures 5–7), and in the Fe^{13+} to Fe^{10+} ionic density ratio, and thus T_e between our three eclipse observing sites (see Figures 10 and 11 and Section 3.2.3). Changes in the inferred T_e are significant to $>3\sigma$ throughout a large portion of the corona (based on photometric and calibration uncertainties, see Section 2.2), with some regions changing by as much as $>10\sigma$. In general, we find that around streamers the corona is increasing in temperature by up to 0.7 $\times$ 10^5 K, while the outer corona is cooling down by as much as 1.0 $\times$ 10^5 K. The same general behavior is present over every time difference, with the largest changes corresponding to the longest time period between the first and last site.

Since a RV of $\approx$190 km s^{-1} for Fe XI and $\approx$280 km s^{-1} for Fe XIV will shift the line emission out of our narrowband observations (see Section 3.1), the line to continuum ratio and T_e metrics will be highly sensitive to velocity perturbations in the corona. The inferred density and temperature changes do not necessarily require that specific plasma change its kinetic electron temperature, but can rather be explained if the corona is disturbed enough to change the average plasma distribution along the line of sight with a Doppler velocity less than about 200 km s^{-1}. Additionally, a radial outflow speed of only 200 km s^{-1} would result in a travel distance of 0.5 $R_\odot$ over the half hour from Mitchell, OR to Alliance, NE. So it is possible for much of the corona to substantially change its density and temperature distribution along a single line of sight during that time because we are not really observing the exact same plasma at each site.

The most likely cause of the inferred line emission and T_e changes is the set of eruptions that took place just prior to the time of the eclipse (see Section 2.3). CMEs have previously

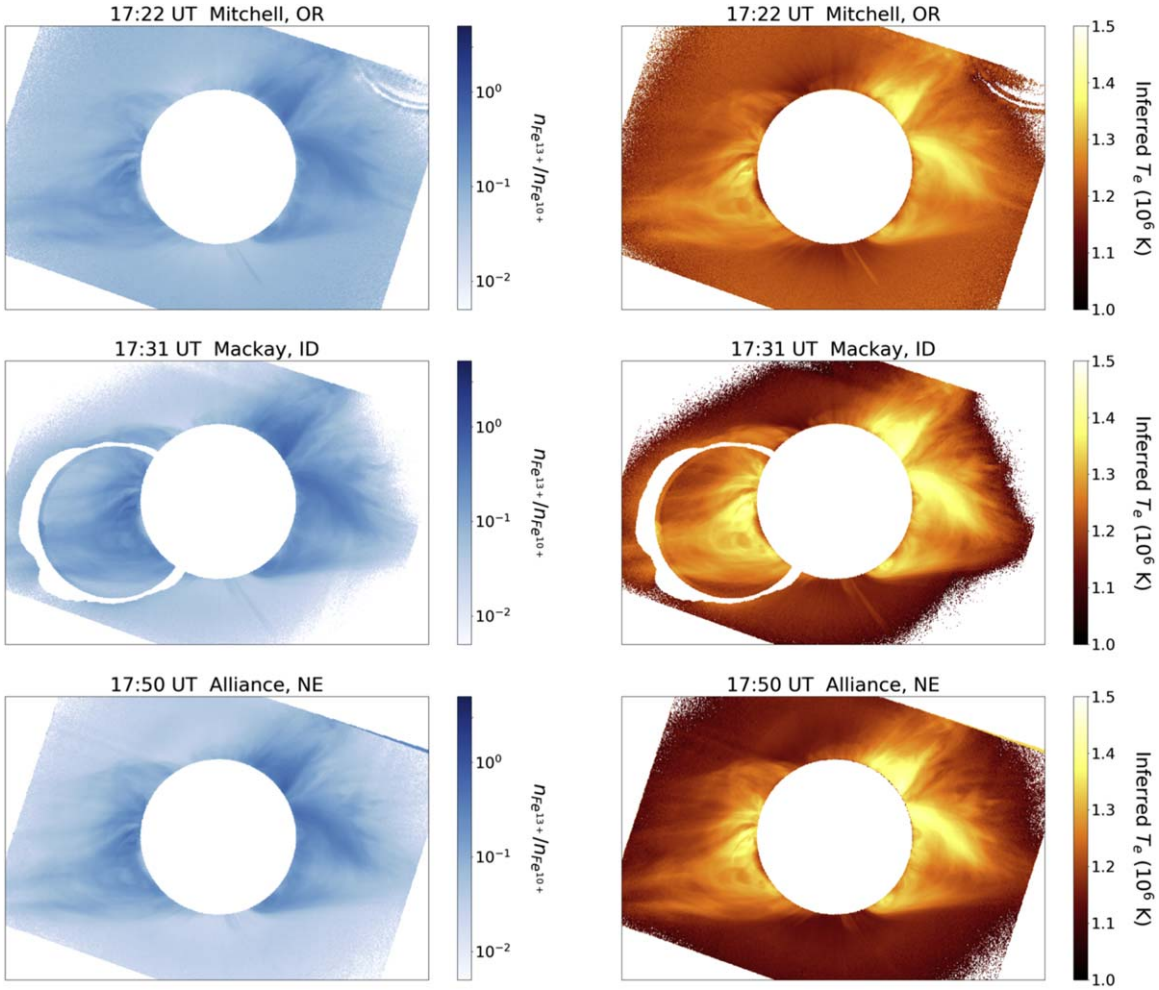

Figure 10. Left: Density ratio of Fe $^{13+}$ to Fe $^{10+}$ as calculated using Equation (9) (see Section 3.2.3) from the observations of Fe XI and Fe XIV made at three separate sites. Right: Inferred electron temperature (T_e) from the relative density measurements that were fed through the temperature function shown in Figure 9. The white ring in the middle panels indicates the location of a ghost image as in Figure 5.

been shown to have secondary "sympathetic CMEs" that commonly occur elsewhere in the corona in the first few hours after an initial eruption event (Moon et al. 2003). Sympathetic CMEs are thought to be caused by magnetically connected regions near the solar surface, such as filaments and active regions, where a CME in one region can stimulate connected regions to erupt. The dynamics of the small eruptive events of the two western streamers can be explained in this manner. It is likely that they would not have erupted on their own, and indeed they were stable enough to not generate a CME. Instead, the perturbation from the CME in the SE, combined with the erupting active region near disk center, caused them to undergo a minor sub-CME (i.e., failed CME) scale eruption. At the time of the Mitchell, OR, the corona was observed in the period immediately following these eruptions. Therefore, it is likely that we have observed the corona recovering from the eruptive perturbations.

The observations at Mitchell occurred 4 hours after the beginning of the CME activity. Consequently, the Mitchell data do not truly represent the initial conditions of the corona without a CME present. It is thus somewhat difficult to interpret the exact physical cause of the line to continuum ratio and T_e changes, as the changes are relative to an already perturbed state. One possible interpretation is that a CME shockwave passed through the corona prior to our first observation. Consequently, the abundance of Fe XIV may have been enhanced in the Mitchell data. The decrease of Fe XIV in the coronal holes would then represent the departure of this plasma from the corona (or at least accelerated to a Doppler velocity $>200\,\mathrm{km\,s^{-1}}$). An increasing Fe XIV in the lower regions of the streamers could then be explained as either heating from the CME activity or by the magnetic field lines in the streamers repairing themselves by re-closing field lines that were ripped open by the CMEs (which would increase the density of hot plasma).

Similarly, the Fe XI intensity may have been suppressed at the time of Mitchell, so the increase may be due to cold plasma repopulating the plane of the sky after the CME disturbed it. The location of the largest increase of Fe XI intensity is just below the CME front in the south-western corona, which supports this interpretation. However, the Fe XI changes are relative to the northern coronal hole (due to calibration issues, see Section 2.2). If the Fe XI intensity was actually dropping in the coronal hole, then the interpretation of the data would be somewhat different. Regardless, we can say with confidence that there were dramatic changes in the corona on short timescales and that CME activity is the driving cause.

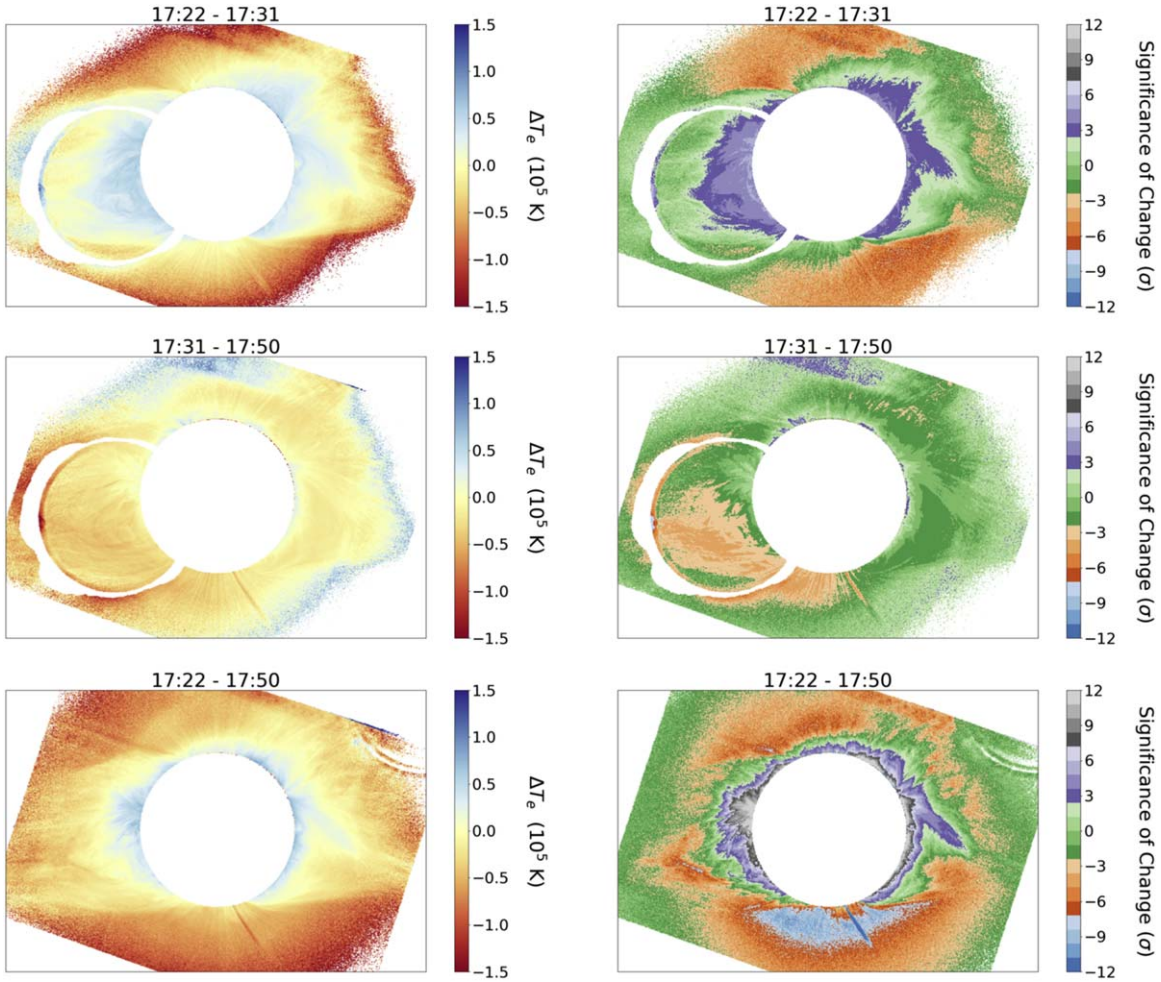

Figure 11. Changes in the inferred T_e (left) between each of the three sites (see Section 3.2.3). Top: Mackay–Mitchell; Middle: Alliance–Mackay; Bottom: Alliance–Mitchell. The white rings in the top and middle panels are the same indication of a ghost image as in Figure 5.

Even though the CME and sub-CME eruptive events that occurred prior to the eclipse were not strikingly large in either LASCO or AIA data, these events caused significant changes to the thermodynamics of coronal plasma on a scale of only 10–30 minutes. Small scale CMEs have previously been found to have a substantial impact on the structure and brightness of field lines in the corona using TSE white light data (similar to Figure 1(A), Alzate et al. 2017), but never before have CMEs been shown to have such a global impact on the electron temperature and density within the corona below 3 $R_\odot$. Future modeling efforts should strive to explain the cause of such rapid CME-driven changes in the mid-corona.

While such changes have never been reported directly in the corona, CMEs have been shown to have substantial impacts in the heliosphere. Studies using in situ detectors have long found shock waves resulting from CMEs in interplanetary space (e.g., Gosling et al. 1968; Hundhausen et al. 1970). Ionic state measurements have indicated that CME shock fronts do increase the ionization state of solar wind particles, and so will increase the inferred coronal T_e of such events (e.g., Bame et al. 1979; Fenimore 1980). The interpretation of the dynamics in the corona has been limited because of the difficulty in robustly tracing back in situ measurements to precise sources in the corona (Galvin 1997).

Direct observations in the corona during TSEs, as presented here, are currently the best technique to probe the temperature dynamics in the solar corona between 1 and 3 $R_\odot$. Even the new generation of ground-based solar telescopes such as DKIST will not be able to measure such rapid and global changes in the corona as we have presented in this study, due to their limited spatial extent.

5. Conclusions

In this work, we have presented observations of the Fe XI and Fe XIV optical forbidden line emission between 1 and 3 $R_\odot$ from three different sites taken during the 2017 August 21 TSE (see Section 2.1). The line to continuum ratio (Figure 5) was determined for each ion at each site and used to infer the relative density of Fe^{10+} and Fe^{13+} (Figure 10), and then compute a coronal electron temperature (T_e) via theoretical abundances (as described in Section 3.2.3). We find that:

1. T_e in the corona ranges from 1.1 to 1.4 $\times$ 10^6 K. Open field line structures such as coronal holes have the lowest temperatures ((1.1–1.2) $\times$ 10^6 K), while streamers have the hottest temperatures ((1.2–1.4) $\times$ 10^6 K). These results are consistent with previously published inferences (see references in Section 4).
2. Statistically significant temporal changes of the line to continuum intensity ratio of Fe XIV (Figure 6) and Fe XI (Figure 7), and of T_e (Figure 11) occur throughout the corona over the 28 minutes between the first and last

observing site. The outer corona is decreasing in temperature (up to 10^5 K), while the inner corona is increasing in temperature (up to 0.7×10^5). Almost the entire corona had the inferred T_e change by $>3\sigma$, with a sizable fraction changing by $>10\sigma$. These changes are likely due to the impact of a CME and two smaller eruptions just prior to the eclipse (see Sections 2.3, 4.2).

3. When observing emission lines at visible wavelengths, it is critical to measure the corresponding continuum radiation to subtract electron scattering (i.e., K corona) and scattering by interplanetary dust (i.e., F corona) to correctly isolate ionic emission (see Section 2.1). Even in a small bandpass, the continuum radiation constitutes a substantial fraction of the emission at optical wavelengths. We thus caution the "spectral purity" arguments of Bemporad et al. (2017), who state that correction for the continuum is not necessary. Indeed, using an on-band observation alone will not produce physically meaningful results (especially for Fe XIV, see Section 3.1).

This work highlights the value of multi-site narrowband imaging for inferring T_e via charge state ratios throughout the corona, and its temporal evolution. If ground- or space-based coronagraph telescopes are equipped with a similar suite of filters, as used in this work, then inferences of T_e and the impact of dynamic events such as CMEs could be studied with high cadence and over long periods of time with the same techniques demonstrated here.

Special thanks go to Judd Johnson for designing and building the narrowband camera systems used in this work. We thank Martina Arndt, Garry Nitta, Marcel Bélík and Radovan Mrllák for their assistance in operating the narrowband camera systems during totality. Thanks also to Nathalia Alzate and Huw Morgan for sharing the processed *SDO*/AIA and *SOHO*/LASCO-C2 images (in Figure 2). Financial support was provided by NASA grant NNX17AH69G and NSF grants AGS-1358239, AGS-1255894, and AST-1733542 to the Institute for Astronomy of the University of Hawaii. AAS provided partial support to S.H. with grant ORS001869, and auRA/NSO supported B.B. under grant N97991C to the Institute for Astronomy at the University of Hawaii. M.D. was supported by the Grant Agency of Brno University of Technology, project No. FSI-S-14-2290.

Appendix A
Doppler Shifted Line Emission

A blueshift Doppler velocity of $\approx$530 km s^{-1} can contribute additional Doppler shifted ionic emission in the continuum bandpass used at Mackay and Alliance. We can expect possible emission from the Fe XI line at that velocity because Fe^{10+} is highly abundant in the fast solar wind ($> \approx 600$ km s^{-1}, e.g., Smith et al. 2003; Habbal et al. 2010b). The Fe^{13+} ion is much more abundant in the slow solar wind (between 200 and 600 km s^{-1}), so Fe XIV emission is possible but not as likely in large quantities at a velocity of 530 km s^{-1}.

Thankfully, the Mitchell data are pristine (see Section 2.2) and we had an additional 552.3 nm continuum observation that we used as a direct substitute for the Fe XIV continuum at the Alliance site. To utilize "green" continuum observations for the Fe XI 789.2 nm line, we first had to account for any reddening in the corona due to dust scattering of the F corona (see Section 2.1). We measured the coronal color by taking the continuum intensity ratio for the Mitchell 527.4 nm and 786.1 nm data, after a relative calibration in the western streamer below 1.1 $R_\odot$ (where the K corona dominates). The resulting reddening map is presented in Figure 12. The Mackay and Alliance Fe XI continuum data were then generated by using green continuum data with an enhancement from the F corona reddening map (see Section 2.2 for details on the

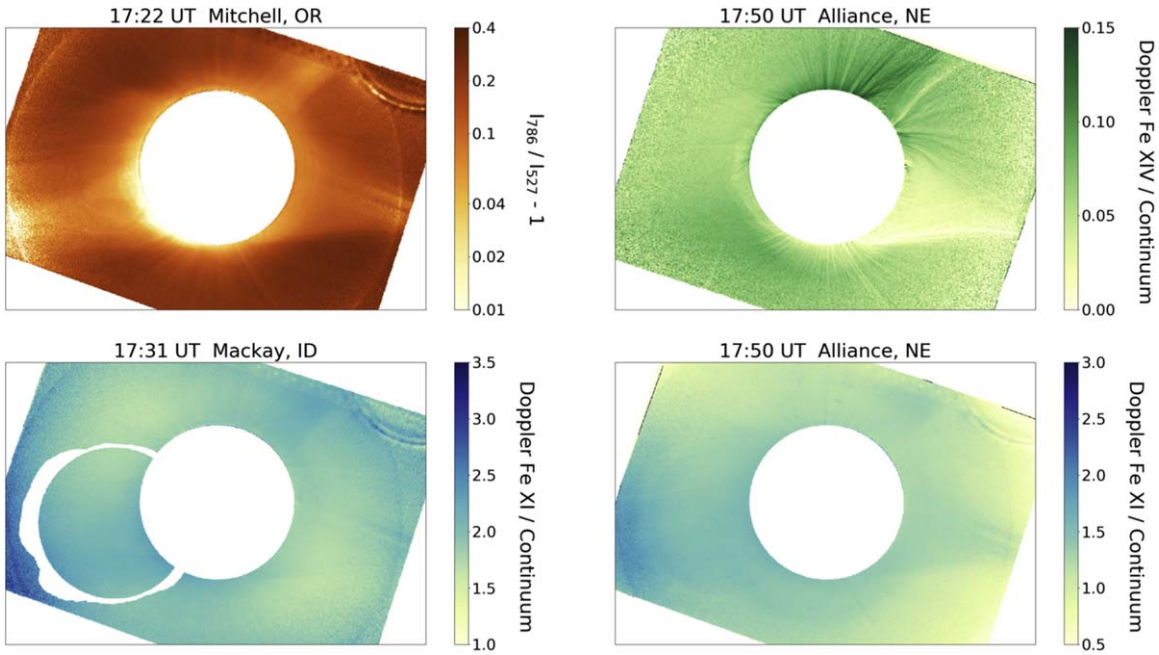

Figure 12. Top left: Excess of emission at 786 nm compared to 527 nm at Mitchell. Top right: Doppler shifted ($\approx$530 km s^{-1}) line to continuum ratio of Fe XIV measured at Alliance. Bottom left: Doppler shifted line to continuum ratio of Fe XI from Mackay. Bottom right: Same as left but for Alliance. The line and continuum data were calibrated using the technique outlined in Section 2.2. The white ring in the middle panels indicates the location of a ghost image in the raw data produced by internal reflections in the optics (see Appendix B).

calibrations and generation of the synthetic continuum data for Mackay and Alliance).

Once new continuum data had been created for the line emission observations at Mackay and Alliance, we were able to measure the quantity of Doppler emission in the original off-band data. Removing the 552.3 nm continuum from the Alliance data indicates a small amount of Doppler shifted Fe XIV emission, with an average intensity of 5.7% relative to the continuum (see Figure 12). The location of the largest Doppler shifted Fe XIV intensity matches the location of the decreasing Fe XIV emission in the plane of the sky coronal holes (see Section 3.1). The largest Doppler emission in the north coronal hole could also be caused by the halo-CME originating from the central disk active region, which was at a latitude of about 10° north. A halo-CME from that active region would likely be pointed slightly northward and would explain the structure of the Doppler shifted Fe XIV observation. Given the small amount of Doppler shifted Fe XIV emission: we used the possibly contaminated Fe XIV continuum at Mackay, but added an extra 5.7% uncertainty to the Mackay data.

The Fe XI Doppler emission had a much stronger intensity than Fe XIV (see Figure 12), with some lines of sight having a Doppler emission intensity of 3 times that of the continuum. Given the 0.5 nm width of the bandpasses, the Doppler observations will observe emission contributions from everything between about 350 and 700 km s^{-1}, which explains why the Doppler emission can still be stronger than the continuum. The Mackay data has a higher Fe XI Doppler intensity throughout (about a 10%–30% difference), but both Mackay and Alliance have the same basic structure of the highest emission occurring at the location of the western CME (see Figure 12). Since the CME is emitting Fe XI at 530 km s^{-1}, the velocity vector of the CME has to be somewhat out of the plane of the sky. Such a vector would also explain why the CME was not reported as a major event by LASCO coronagraph data (see Section 2.3). Nonetheless, continuum intensity variation in the LASCO-C2 data around the time of the eclipse does support halo-CME activity (see Figure 4). The overall Doppler Fe XI intensity decrease between Mackay and Alliance hints that either the CME was passing through this velocity space temporarily (i.e., the CME may have been accelerating), or that the ionic emission is decreasing as the CME expands. The *ACE* spacecraft also saw a CME signature three days after the eclipse that supports the presence of a halo-CME (see Section 2.3). The CME arrival time delay would correspond to a constant velocity of about 545 km s^{-1} if the CME began at 13:00 UT on the day of the eclipse, which is consistent with the observed Doppler shifted emission.

Appendix B
Ghost Image Removal

In some of the narrowband imaging cameras, internal reflections from the optics resulted in the appearance of secondary "ghost" images of the corona on the detector. The ghost images are significantly fainter, typically $\leqslant$2% of the

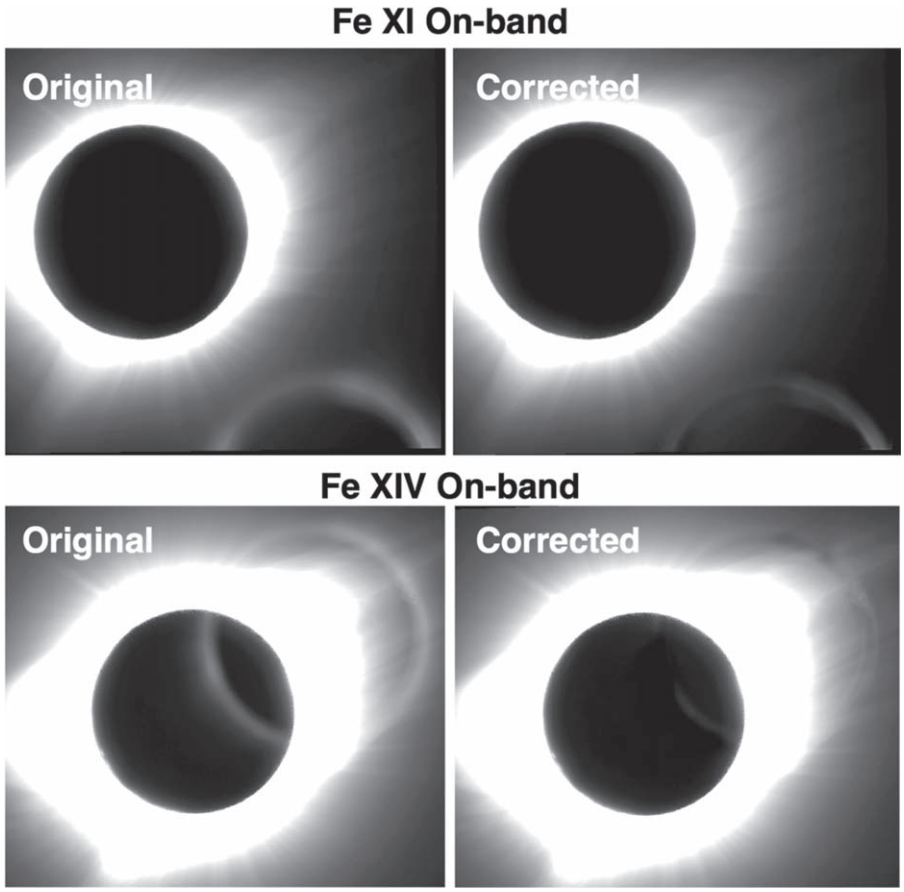

Figure 13. Example of the ghost image removal on Fe XI (top) and Fe XIV (bottom) on-band data (not off-band subtracted) from the Mackay, ID site. The left-hand column shows a cropped version of the original images with logarithmic scaling and somewhat saturated in order to show the ghost images clearly. The final ghost subtracted images are shown on the right with scaling identical to the original images.

original intensity. Fortunately, the intensity of the corona drops exponentially with distance from the Sun, so only the inner portion of the reflected corona has any substantial intensity in the ghost images. Unfortunately, there will be a small systematic bias due to the ghost image between ≈1 and 1.5 $R_{\odot}$.

To correct for the bias caused by the ghost image, we removed the signature of ghost images by modeling the reflection and subtracting it. Given that the ghost is a reflection of the original image, we subtracted the image from itself with a physical offset (δX, δY) and an intensity multiplier to simulate the brightness of the ghost (B_g). We also accounted for the ghost image being out of focus by smoothing the original image with a Gaussian filter using $\sigma = \sigma_g$ and rotated the ghost frame by 180° before subtraction, to account for the rotation of the mirrored image caused by the telescope's internal optics (a double mirror reflection in the narrowband filter). We first set the parameters manually then allowed perturbations in an automated Monte Carlo brute force technique to improve the ghost subtraction.

Samples of the ghost removal results are shown in Figure 13, with frames from before and after the subtraction. This technique is not perfect and it often leaves visible traces of the ghost image, especially in a ring that corresponds to the reflection of the bright inner corona. The benefit of doing this subtraction method is to remove systematic bias that the ghost image has outside of the obvious ghost ring.

We successfully performed this removal process to ghost images in the far corners of the Mitchell Fe XIV off-band, Mackay Fe XI on-band and Alliance Fe XIV on-band images, which had no visible effect on our results. Ghost images were also removed from the Alliance Fe XI off-band and Mackay Fe XIV on-band images, which had more centrally located ghost reflections. The Alliance Fe XIV ghost was very faint and could be removed almost completely, leaving only a very slight sign of the ring. Unfortunately, the inner ring of the ghost image in the Mackay Fe XIV on-band data (shown in Figure 13) still had a large amount of contamination, due to the brightness of the ghost image. We masked the region of the Mackay Fe XIV ghost image where the ghost ring had substantially contaminated the image to reduce the chances of misinterpretation that the ghost ring is some real physical structure. The masked ring can be seen in the panels involving Mackay data, specifically Figures 5–7, 10–12.

ORCID iDs

Benjamin Boe https://orcid.org/0000-0002-6396-8209
Shadia Habbal https://orcid.org/0000-0003-4089-9316
Adalbert Ding https://orcid.org/0000-0001-6573-7810

References

Alfvén, H. 1947, MNRAS, 107, 211
Alzate, N., Habbal, S. R., Druckmüller, M., Emmanouilidis, C., & Morgan, H. 2017, ApJ, 848, 84
Arnaud, M., & Raymond, J. 1992, ApJ, 398, 394
Bame, S. J., Asbridge, J. R., Feldman, W. C., Fenimore, E. E., & Gosling, J. T. 1979, SoPh, 62, 179
Bemporad, A., Pagano, P., Giordano, S., & Fineschi, S. 2017, ExA, 44, 83
Boe, B., Habbal, S., Druckmüller, M., et al. 2018, ApJ, 859, 155
Boerner, P., Edwards, C., Lemen, J., et al. 2012, SoPh, 275, 41
Borrini, G., Gosling, J. T., Bame, S. J., & Feldman, W. C. 1982, JGR, 87, 7370
Cranmer, S. R., van Ballegooijen, A. A., & Edgar, R. J. 2007, ApJS, 171, 520
Druckmüller, M. 2009, ApJ, 706, 1605
Druckmüller, M. 2013, ApJS, 207, 25
Druckmüller, M., Rušin, V., & Minarovjech, M. 2006, CoSka, 36, 131
Dudok de Wit, T., Moussaoui, S., Guennou, C., et al. 2013, SoPh, 283, 31
Edlén, B. 1943, ZAp, 22, 30
Fenimore, E. E. 1980, ApJ, 235, 245
Fletcher, L., Dennis, B. R., Hudson, H. S., et al. 2011, SSRv, 159, 19
Galvin, A. B. 1997, GMS, 99, 253
Gloeckler, G., Cain, J., Ipavich, F. M., et al. 1998, SSRv, 86, 497
Gloeckler, G., Geiss, J., Balsiger, H., et al. 1992, A&AS, 92, 267
Gosling, J. T., Asbridge, J. R., Bame, S. J., Hundhausen, A. J., & Strong, I. B. 1968, JGR, 73, 43
Grotrian, W. 1934, ZAp, 8, 124
Grotrian, W. 1939, NW, 27, 214
Habbal, S. R., Druckmüller, M., Morgan, H., et al. 2010a, ApJ, 719, 1362
Habbal, S. R., Esser, R., & Arndt, M. B. 1993, ApJ, 413, 435
Habbal, S. R., Morgan, H., & Druckmüller, M. 2014, ApJ, 793, 119
Habbal, S. R., Morgan, H., Druckmüller, M., & Ding, A. 2010b, ApJL, 711, L75
Habbal, S. R., Morgan, H., Johnson, J., et al. 2007, ApJ, 663, 598
Harra, L. K., Sakao, T., Mandrini, C. H., et al. 2008, ApJL, 676, L147
Herzberg, G. 1945, Atomic Spectra and Atomic Structure (New York: Dover Press)
Hundhausen, A. J., Bame, S. J., & Montgomery, M. D. 1970, JGR, 75, 4631
Hundhausen, A. J., Gilbert, H. E., & Bame, S. J. 1968, ApJL, 152, L3
Kimura, H., & Mann, I. 1998, EP&S, 50, 493
Ko, Y.-K., Fisk, L. A., Geiss, J., Gloeckler, G., & Guhathakurta, M. 1997, SoPh, 171, 345
Koutchmy, S., & Lamy, P. L. 1985, in IAU Coll. 85: Properties and Interactions of Interplanetary Dust, ed. R. H. Giese & P. Lamy (Dordrecht: Reidel), 63
Kramida, A., Ralchenko, Yu., & Reader 2018, NIST Atomic Spectra Database (ver. 5.6.1) (Gaithersburg, MD: National Institute of Standards and Technology) [Online]. Available: https://physics.nist.gov/asd [2019, February 5]
Landi, E., Gruesbeck, J. R., Lepri, S. T., Zurbuchen, T. H., & Fisk, L. A. 2012, ApJ, 761, 48
McComas, D. J., Bame, S. J., Barraclough, B. L., et al. 1998, GeoRL, 25, 1
Meftah, M., Damé, L., Bolsée, D., et al. 2018, A&A, 611, A1
Moon, Y.-J., Choe, G. S., Wang, H., & Park, Y. D. 2003, ApJ, 588, 1176
Morgan, H. 2015, ApJS, 219, 23
Morgan, H., Byrne, J. P., & Habbal, S. R. 2012, ApJ, 752, 144
Morgan, H., & Druckmüller, M. 2014, SoPh, 289, 2945
Morgan, H., & Habbal, S. R. 2007, A&A, 471, L47
Morgan, H., & Taroyan, Y. 2017, SciA, 3, e1602056
O'Dwyer, B., Del Zanna, G., Mason, H. E., Weber, M. A., & Tripathi, D. 2010, A&A, 521, A21
Owocki, S. P., Holzer, T. E., & Hundhausen, A. J. 1983, ApJ, 275, 354
Parker, E. N. 1958, ApJ, 128, 664
Raymond, J. C., Kohl, J. L., Noci, G., et al. 1997, SoPh, 175, 645
Roeser, S., & Staude, H. J. 1978, A&A, 67, 381
Sakao, T., Kano, R., Narukage, N., et al. 2007, Sci, 318, 1585
Smith, E. J., Marsden, R. G., Balogh, A., et al. 2003, Sci, 302, 1165
Stone, E. C., Frandsen, A. M., Mewaldt, R. A., et al. 1998, SSRv, 86, 1
van de Hulst, H. C. 1947, ApJ, 105, 471
van de Hulst, H. C. 1950, BAN, 11, 135
Young, C. A. 1870, Natur, 1, 532
Young, C. A. 1871, Natur, 4, 445
Young, C. A. 1872, Natur, 7, 28
Zurbuchen, T. H., Fisk, L. A., Gloeckler, G., & von Steiger, R. 2002, GeoRL, 29, 1352